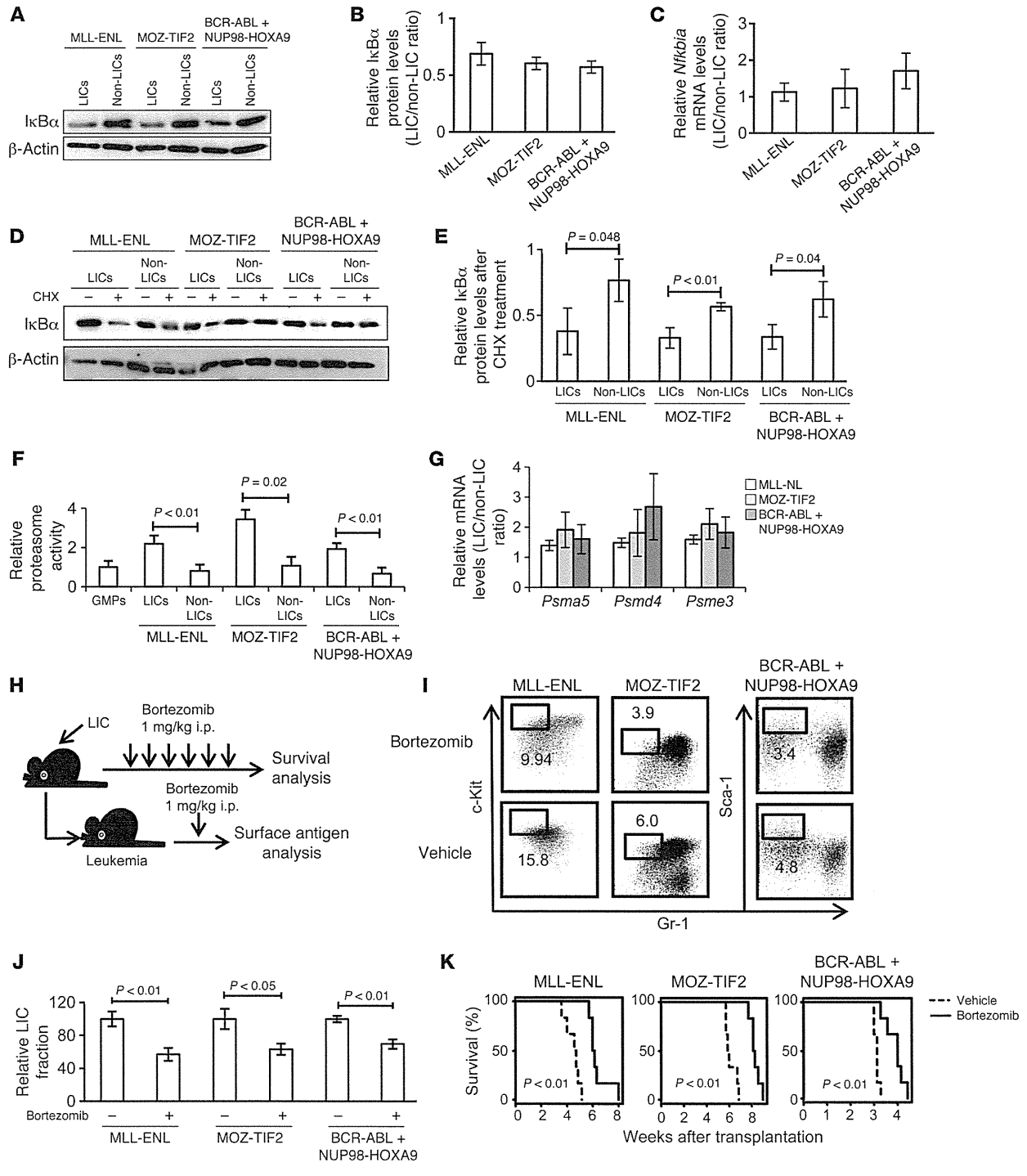

Figure 5
LICs have higher proteasome activity than non-LICs. (**A** and **B**) Immunoblotting of IκBα in LICs and non-LICs (**A**). Protein levels were quantified with ImageJ software (**B**). Data representative of four experiments with SD are shown. (**C**) Relative mRNA expression of *Nfkbia* in LICs compared with that in non-LICs ($n = 4$ each). Error bars indicate SD. (**D** and **E**) Immunoblotting of IκBα in LICs and non-LICs. Cells were pretreated with MG132 for 1 hour and incubated for an additional hour with or without cycloheximide (CHX) (**D**). IκBα protein levels were quantified with ImageJ software, and the relative decrease in IκBα after cycloheximide treatment was calculated ($n = 3$ each). Error bars indicate SD (**E**). (**F**) Analysis of 20S proteasome activity quantified with fluorescence produced upon cleavage of the proteasome substrate SUC-LLVY-AMC ($n = 4$ each). Error bars indicate SD. (**G**) Relative mRNA expression of proteasome subunits in LICs compared with that in non-LICs ($n = 4$ each). Error bars indicate SD. (**H**) Schematic representation of the experiments. Each type of LIC was secondarily transplanted into mice. Bortezomib was injected twice weekly or injected once after incidence of leukemia. (**I** and **J**) Comparison of surface marker profiles in leukemic mice treated with bortezomib or vehicle. Representative FACS data (**I**) and relative percentages of Gr-1^{lo} c-Kit^{hi} fraction in MLL-ENL– or MOZ-TIF2–induced leukemic mice, and Gr-1^{lo}Sca-1^{hi} fraction in BCR-ABL/NUP98-HOXA9–induced leukemic mice are shown ($n = 3$ each) (**J**). Values of control mice were normalized to 100%. Error bars indicate SD. (**K**) Survival curves of mice in the experiments shown in **H** ($n = 6$ each).

progression. Unveiling the role of TNF-α as a paracrine mediator would further extend the therapeutic options for AML.

Few studies have compared the NF-κB activity of different fractions within leukemia cells, and the mechanism underlying the difference in this activity has not been analyzed (44). We focused on proteasome activity as the essential machinery supporting NF-κB activity in LICs. Although high proteasome activity has been reported in various types of cancers (45, 46), its actual role in the malignant phenotype remained to be elucidated. In this study, we found that proteasome activity was especially high in LICs, which contributed to selective NF-κB activity in LICs via the efficient degradation of IκBα. Conversely, the inefficient NF-κB nuclear translocation we observed in non-LICs, despite TNF-α–enriched leukemic BM cells, could be explained by the low proteasome activity in these cells. Therefore, we postulate that both an activating stimulus such as TNF-α and high proteasome activity are required for efficient NF-κB signaling (Figure 7F). Both of these conditions are present exclusively in LICs, which acquire selective NF-κB activation. We also found that the expression levels of proteasome subunit genes were elevated in LICs compared with those in non-LICs, genes that could be involved in regulating proteasome function. Because we observed similar expression patterns in LICs and non-LICs in human AML cells, an elevated expression level of proteosome subunit genes might be one of the common characteristics of the LIC phenotype. Further studies will be needed to elucidate the regulatory mechanism of the proteasome gene families.

Our findings provide several advantages when considering their application to the clinical care setting. First, an activated NF-κB/TNF-α feedback loop was seen in AML LICs that had different genetic abnormalities. Although the therapeutic strategy of targeting aberrant molecules based on genetic abnormalities such as FLT3-ITD is promising, its application is limited to a particular group of patients. In contrast, inhibition of the NF-κB signal in addition to standard chemotherapy would show beneficial effects in most AML patients. Second, because there was a strong positive correlation between the NF-κB signal and TNF-α secretion, therapeutic efficacy could easily be inferred from the abundance of TNF-α instead of from evaluation of the activation status of NF-κB. Third, the NF-κB/TNF-α signal and enhanced proteasome activity are selectively seen in LICs, but not in normal HSCs. A recent study has shown that complete ablation of p65 in hematopoietic cells attenuates the long-term capacity for hematopoietic reconstitution (47). However, our data from the experiments in which we introduced IκB-SR into normal BM cells show that partial repression of NF-κB activity exerted minimal influence on normal hematopoiesis, while it markedly inhibited leukemia progression. These results indicate that there is a therapeutic window during which LICs can selectively be killed by NF-κB inhibition without seriously affecting normal hematopoiesis. Alternatively, there is some evidence that TNF-α has suppressive effects on normal HSCs (48, 49). The opposing role of TNF-α in LICs and HSCs is additionally beneficial, since anti–TNF-α therapy contributes to the recovery of normal hematopoiesis and attenuates LIC proliferation. Now that the TNF-α antagonist etanercept is widely used in inflammatory diseases such as rheumatoid arthritis, this drug might be a promising candidate for treating patients with AML.

In summary, the present study shows that blocking the NF-κB pathway offers a promising therapeutic approach for targeting LICs in various types of myeloid leukemia, without disturbing normal hematopoiesis. We further determined that autocrine TNF-α signaling and enhanced proteasome activity are crucial for maintaining constitutive NF-κB activity in LICs, findings that may also provide a new therapeutic opportunity.

Methods

Animals. C57BL/6 mice and BALB/c mice were purchased from Japan SLC, Inc. *Tnf*-knockout mice on a BALB/c background were established as described previously (50). *Rela*-floxed mice on a C57BL/6 background were provided by H. Algül and R.M. Schmid (32). BALB/c mice were used as the controls in the experiments using *Tnf*-knockout mice, and C57BL/6 mice were used in the other experiments.

Retrovirus production and BM transplantation assays. To obtain retrovirus supernatants, platinum-E (Plat-E) packaging cells were transiently transfected with each retrovirus vector, and the viral supernatants were collected 48 hours after transfection and used immediately for infection. To establish each myeloid leukemia mouse model, we used pMSCV-neo-MLL-ENL; pMSCV-MLL-ENL-internal ribosome entry site–*EGFP* (*IRES-EGFP*); pGCDNsam-MLL-ENL-*IRES*-Kusabira-Orange; pGCDNsam-MOZ-TIF2-*IRES-EGFP*; pGCDNsam-MOZ-TIF2-*IRES*-Kusabira-Orange; pGCDNsam-BCR-ABL-*IRES-EGFP*; pGCDNsam-BCR-ABL-*IRES*-Kusabira-Orange; and pMSCV-neo-NUP98-HOXA9. GMPs isolated from the BM of 8- to 10-week-old mice were transduced with the respective vectors and injected into sublethally irradiated (7.5 Gy) recipient mice. For experiments involving the generation of leukemia cells with IκB-SR, MLL-ENL leukemia cells were transduced with pBabe-GFP or pBabe-GFP-IκB-SR. MOZ-TIF2, and BCR-ABL/NUP98-HOXA9 leukemia cells were transduced with pGCDNsam-Kusabira-Orange or pGCDNsam-IκB-SR-IRES-Kusabira-Orange. For experiments involving the deletion of p65 in *Rela*-floxed mice, leukemia cells were established using Kusabira-Orange–containing retroviral vectors. The developed leukemia cells were transduced with pGCDNsam-EGFP or pGCDNsam-iCre-EGFP and transplanted into sublethally irradiated mice.

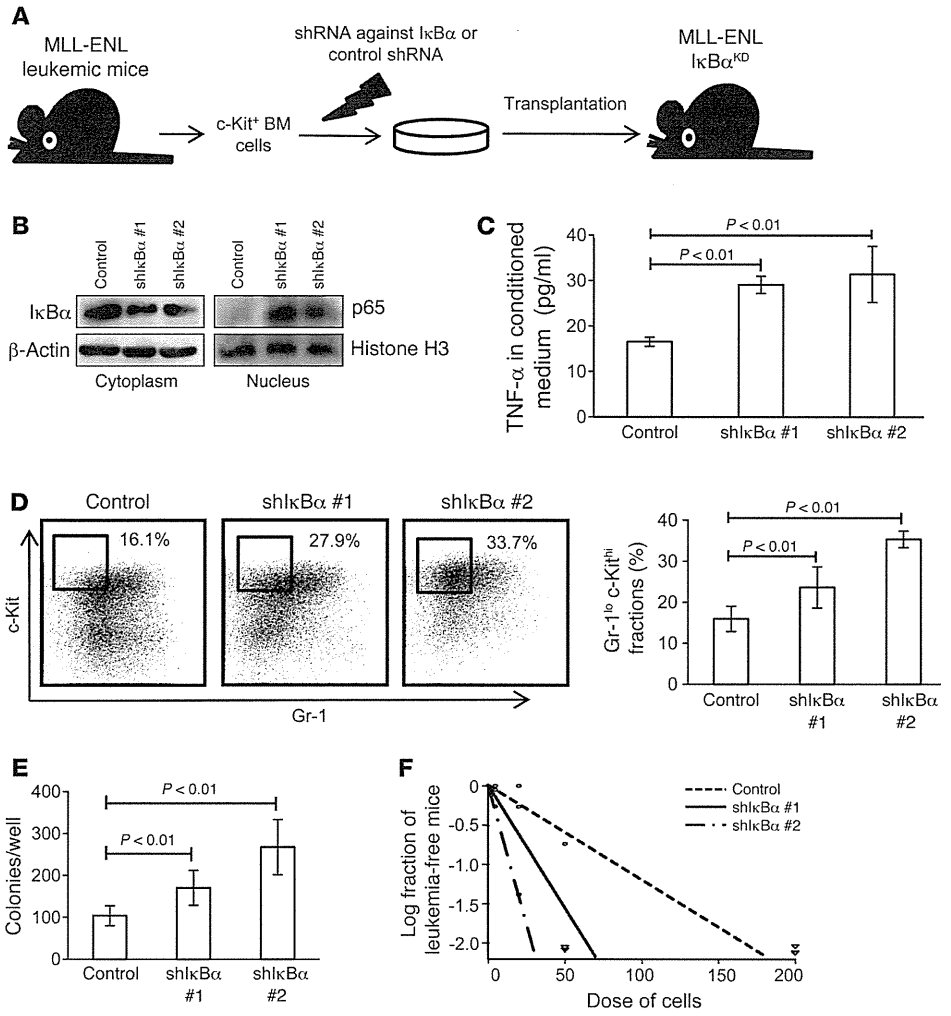

Figure 6
Forcible maintenance of NF-κB activity in leukemia cells enhances LIC frequency. (**A**) Schematic representation of the experiments. c-Kit+ BM cells isolated from MLL-ENL leukemic mice were transduced with shRNA against IκBα or control shRNA and transplanted into sublethally irradiated mice. (**B**) Immunoblotting of cytoplasmic IκBα and nuclear p65 in BM mononuclear cells from MLL-ENL-IκBα^{KD} mice compared with those from control leukemic mice. (**C**) TNF-α secretory ability of MLL-ENL-IκBα^{KD} leukemia cells compared with that of control leukemia cells (n = 4 each). Error bars indicate SD. (**D**) Surface marker profiles of MLL-ENL leukemic mice with or without knockdown of IκBα. Representative FACS plots and mean percentages of Gr-1^{lo}c-Kit^{hi} fractions (n = 6 each). (**E**) CFC assay of MLL-ENL leukemia cells with or without knockdown of IκBα (n = 6). Cells were seeded at 500 cells per well. Error bars indicate SD. (**F**) LIC frequency in BM mononuclear cells derived from MLL-ENL-IκBα^{KD} leukemic mice compared with those from control mice as determined by limiting dilution transplantation assay.

In vivo limiting dilution assays. Varying numbers of cells from different populations were transplanted into sublethally irradiated mice and monitored for disease development (see Supplemental Table 1 for the injected cell numbers).

Immunofluorescence and quantification of p65 nuclear translocation. A total of 1 × 10^4 to 5 × 10^4 cells were cytospun onto glass slides. The cells were fixed with 3.7% formaldehyde in PBS for 30 minutes, permeabilized by treatment with 0.2% Triton X in PBS for 10 minutes, and blocked with 1% BSA in PBS for 60 minutes. Then, the slides were incubated with rabbit anti-p65 polyclonal antibody (sc-372; 1:100 dilution; Santa Cruz Biotechnology Inc.) overnight at 4°C, followed by incubation with Alexa Fluor 555 goat anti-mouse IgG (1:250 dilution; Invitrogen) and TO-PRO3 (1:1,000 dilution; Invitrogen) for 90 minutes. For immunofluorescence staining of Kusabira-Orange+ leukemia cells, Alexa Fluor 647 goat anti-mouse IgG (1:250 dilution; Invitrogen) was used as a secondary antibody, and the nucleus was stained with DAPI. After the cells were washed, they were treated with ProLong Gold Antifade Reagent (Invitrogen). Images were acquired using an Olympus FluoView FV10i confocal microscope with a ×60 objective oil immersion lens. The mean intensity of p65 in the nucleus and cytoplasm of each cell was measured within a region of interest (ROI) placed within the nucleus and cytoplasm. Similarly, the background intensity was quantified within an ROI placed outside the cells. All the measurements were performed using FluoView software. The background-subtracted intensity ratio of nucleus/cytoplasm was calculated in more than 50 cells in each specimen, and the average intensity with SD is presented.

Flow cytometry. Isolation of each fraction from normal or leukemic BM cells was performed using a FACSAria II (BD) cell sorter. For isolation of GMPs and KSLs, biotinylated antibodies against Gr-1 (RB6-8C5), CD11b (M1/70), B220 (RA-3-6B2), CD3 (145-2C11), CD4 (GK1.5), CD8 (53-6.7), and TER119 were used for lineage staining. A PerCP-Cy5.5–labeled streptavidin antibody was used for secondary staining, together with APC–anti–c-Kit (2B8), PE-Cy7–anti–Sca-1 (E13-161.7). FITC–anti-CD34 (RAM34), and PE–anti-CD16/32b antibodies (clone 93). The following antibodies were used for isolation of L-GMPs from GFP-containing leukemia cells: APC-Cy7–anti–streptavidin, PE-Cy5–anti–c-Kit (2B8), PE-Cy7–anti–Sca-1 (E13-161.7), Alexa Fluor 647–anti-CD34 (RAM34), and PE–anti-CD16/32b (clone 93). APC-antistreptavidin and PE-Cy7–anti–Sca-1 antibodies (E13-161.7) were used for sorting LICs and non-LICs in the BCR-ABL plus NUP98-HOXA9 leukemia model. See Supplemental Figures 1 and 2 for detailed FACS plots. For analysis of TNF receptor expression in leukemia cells, biotinylated antibodies against TNF receptor I or II (55R-170) and an APC-Cy7–antistreptavidin antibody were used. Analysis was performed using FlowJo software (Tree Star Inc.).

Table 1
Clinical characteristics of the 12 patients with AML and the 5 patients with normal BM findings

Patient no.	Age	Sex	BM findings	Disease status	Type	Cytogenetics	Blast (%)
1	42	M	AML	Untreated	M2	Normal	87
2	62	M	AML	Relapse	M1	47, XY, del(9)(q13q22),+10	96
3	69	M	AML	Untreated	M4	Normal	90
4	58	M	AML	Untreated	M3	46, XY, t(15;17)	63
5	75	M	AML	Untreated	M4	46, XY, inv(16)	27
6	62	F	AML	Untreated	AML-MRC	NA	24.8
7	72	F	AML	Untreated	AML-MRC	Complex	21
8	42	M	AML	Untreated	M4	46, XY, t(11;17)	25
9	66	M	AML	Untreated	M1	46, XY, t(8;21)	85.4
10	73	F	AML	Untreated	AML-MRC	Complex	44.5
11	65	M	AML	Untreated	AML-MRC	46, XY, t(1;3)	53.3
12	73	M	AML	Untreated	M2	46, XY, add(7)	51.5
13	67	F	Normal			Normal	
14	64	F	Normal			Normal	
15	47	F	Normal			Normal	
16	54	M	Normal			Normal	
17	29	M	Normal			Normal	

Real-time quantitative PCR. Real-time quantitative PCR was carried out on the LightCycler480 system (Roche) using SYBR green reagents according to the manufacturer's instructions. The results were normalized to *Gapdh* levels. Relative expression levels were calculated using the 2-ΔΔCt method (51). The following primers were used for real-time PCR experiments: *Gapdh* forward, TGGCCTCCAAGGAGTAAGAA, and reverse, GGTCTGGGATGGAAATTGTG; *Ncf2* forward, CCAGAAGACCTGGAATTTGTG, and reverse, AAATGCCAACTTTCCCTTTACA; *Tnf* forward, TCTTCTCATTCCTGCTTGTGG, and reverse, GGTCTGGGCCATAGAACTGA; *Il15ra* forward, TAAGCGGAAAGCTGGAACAT, and reverse, TGAGGTCACCTTTGGTGTCA; *Litaf* forward, CTCCAGGACCTTACCAAGCA, and reverse, AGGTGGATTCATTCCCTTCC; *Hoxa9* forward, GGTGCCTGCTGCAGTGTAT, and reverse, GTTCCAGCCAGGAGCGCATAT; *Psma5* forward, CGAGTACGACAGGGGTGTG, and reverse, TGGATGCCAATGGCTGTAG; *Psmd4* forward, GTACATGCGGAACGGAGACT, and reverse, TGTGGTCAGCACCTCACAGT; *Psme3* forward, TTTCAGAGAGCGGATCACAA, and reverse, GGTCATGGATATTTAGAATTGGTTC.

siRNA interference. Specific shRNAs targeting murine *Ikba* mRNA were designed and cloned into pSIREN-RetroQ-ZaGreen vectors. Control shRNA is a nonfunctional construct provided by Clontech. The target sequences, from 5′ to 3′, were: CCGAGACTTTCGAGGAAAT (shIκBα number 1), and AGCTGACCCTGGAAAATCT (shIκBα number. 2).

Immunoblotting. Membranes were probed with the following antibodies: anti-IκBα (Cell Signaling Technology), anti-phospho-IκBα (Ser32) (Cell Signaling Technology), anti-p65 (Santa Cruz Biotechnology Inc.), anti-phospho-p65 (Ser536) (Cell Signaling Technology), anti-β-actin (Cell Signaling Technology), and anti-histone H3 (Cell Signaling Technology). Protein levels were quantified with ImageJ software (NIH). To obtain nuclear and cytoplasmic extracts, an Active Motif Nuclear Extract Kit was used according to the manufacturer's instructions. Cycloheximide treatment assay was performed as described previously, with modification (52). Cells were pretreated with MG132 (20 μM) for 1 hour to initially inhibit the proteasomal degradation of IκBα. Cells were washed twice with medium, then cultured with or without 10 μg/ml of cycloheximide for an additional hour and harvested.

CFC assays. In each experiment, cells were plated onto MethoCult GF M3434 medium (STEMCELL Technologies). Colony numbers in each dish were scored on day 7.

Measurement of TNF-α levels in BM extracellular fluid and conditioned media. BM extracellular fluid was obtained by flushing bilateral femurs and tibia of individual mice with 400 μl PBS. The supernatant was collected after centrifugation. To obtain conditioned media, 0.3–1.0 × 10^6 murine leukemia cells or normal GMPs were cultured in RPMI medium containing 10% FBS and 10 ng/ml IL-3. After a 48-hour incubation, the culture supernatants were collected. The concentration of TNF-α was measured using a murine TNF-α ELISA kit (Gen-Probe Diaclone) according to the manufacturer's instructions. Similarly, 0.5 × 10^4 to 2.0 × 10^4 human AML or normal $CD34^+CD38^-$ cells were cultured for 48 hours in RPMI medium containing 10% FBS and 100 ng/ml SCF, IL-3, and thrombopoietin. The concentration of TNF-α in the harvested supernatants was measured with a human TNF-α Quantikine ELISA kit (R&D Systems).

20S proteasome activity. A 20S proteasome activity assay kit (Cayman Chemical) was used to analyze proteasome activity. A total of 5 × 10^4 freshly isolated normal GMPs, LICs, and non-LICs in each model were assayed according to the manufacturer's protocol. As a control, the proteasome activity of each cell was also assayed after the specific proteasome inhibitor epigallocatechin gallate was added. Fluorescence was measured with a Wallac ARVO V (PerkinElmer), and the proteasome activity of each cell type was calculated by subtracting the respective control value.

Bortezomib treatment studies. For in vivo treatment experiments, LICs of each leukemia model were injected into sublethally irradiated mice: 1 × 10^3 cells in the MLL-ENL or BCR-ABL/NUP98-HOXA9 models, and 1 × 10^4 cells in the MOZ-TIF2 model. Bortezomib was administrated i.p. at doses of 1.0 mg/kg twice weekly for 3 weeks. Treatment was started 1 week after transplantation in the MLL-ENL or BCR-ABL/NUP98-HOXA9 models, and 2 weeks after transplantation in the MOZ-TIF2 model. For experiments analyzing changes in LIC populations, bortezomib was administrated i.p. at doses of 1.0 mg/kg into fully developed leukemic mice. GFP^+ BM cells were collected 24 hours after injection, and surface marker profiles were analyzed.

Analysis of microarray data. We analyzed publicly available gene expression microarray data on murine and human samples from the Gene Expression Omnibus (GEO) database (GEO GSE24797, GSE20377, and GSE24006). A set of CEL files were downloaded from GEO and normalized using the JustRMA function from the Affy package 1.22.1 in Bioconductor. To compare expression profiles of the NF-κB target genes, normalized data were tested for GSEA using previously described NF-κB target gene sets (29), and a nominal *P* value was calculated. For screening of genes with elevated expression levels in LICs compared with those in normal HSPCs, the expression values of individual genes were compared between groups. Genes significantly elevated in LICs from all three leukemia models as determined by an unpaired Student's *t* test ($P < 0.05$)

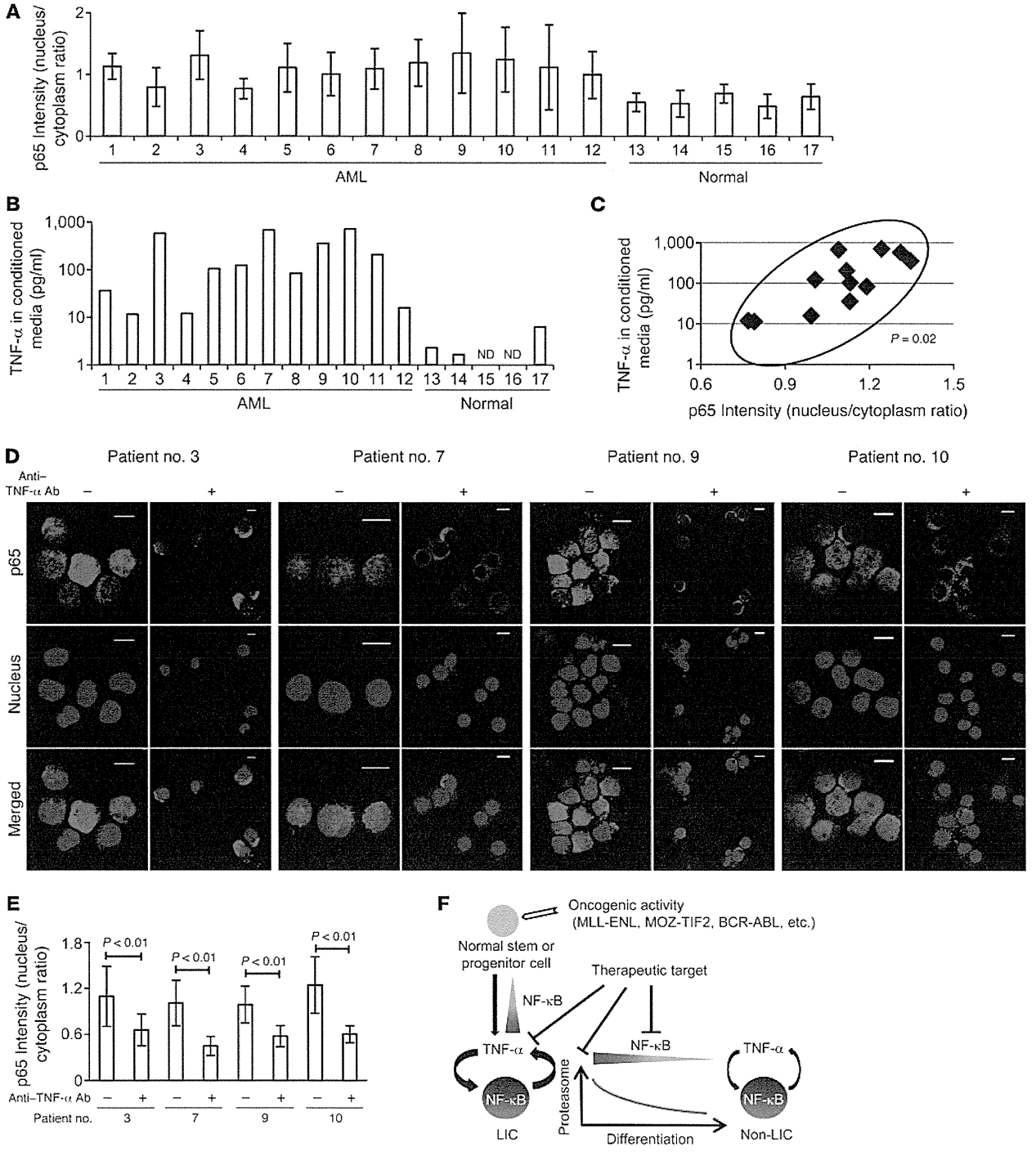

Figure 7

NF-κB/TNF-α positive feedback loop is activated in human AML LICs. (**A**) Quantification of p65 nuclear translocation assessed by the mean nucleus/cytoplasm intensity ratio by immunofluorescence staining. The $CD34^+CD38^-$ fractions isolated from AML or normal BM were analyzed. More than 50 cells were scored in each specimen, and the average intensity ratio with SD is shown. (**B**) TNF-α concentration of culture media conditioned by human AML LICs and normal HSCs measured by ELISA. ND, not detected. (**C**) Correlation between p65 nuclear translocation intensity ratio and TNF-α secretory ability of human AML LICs. (**D**) Immunofluorescence assessment of p65 nuclear translocation in LICs purified from 4 patients after serum-free culture with neutralizing antibody against TNF-α or isotype control. Scale bars: 10 μm. (**E**) Quantification of p65 nuclear translocation of LICs with or without neutralizing antibody against TNF-α assessed by the mean nucleus/cytoplasm intensity ratio. (**F**) Proposed model showing the role of NF-κB signaling in LICs. Positive feedback loop involving NF-κB/TNF-α promotes the maintenance and proliferation of LICs. The signaling is supported by active proteasome machinery, which declines with LIC differentiation.

were selected, among which genes also elevated in human AML LICs (Student's *t* test set at $P < 0.01$) were ultimately selected.

Statistics. Statistical significance of differences between groups was assessed with a 2-tailed unpaired Student's *t* test. Differences were considered statistically significant at a *P* value of less than 0.05. LIC frequency was calculated by Poisson statistics. In leukemia cell transplantation experiments, the overall survival of mice in BM transplantation assays is depicted by a Kaplan-Meier curve. Survival between groups was compared using the log-rank test. To measure the correlation between NF-κB intensity and TNF-α secretion in human AML samples, the Spearman's rank correlation coefficient was used.

Study approval. A total of 12 BM cells derived from patients with AML were obtained from the Department of Hematology and Oncology of the University of Tokyo Hospital. Five BM cells from patients diagnosed with lymphoid neoplasia without BM invasion were used as normal controls. The study was approved by the ethics committee of the University of Tokyo, and written informed consent was obtained from all patients whose samples were collected. All animal experiments were approved by the University of Tokyo Ethics Committee for Animal Experiments.

Acknowledgments

We thank T. Kitamura for the Plat-E packaging cells; H. Nakauchi and M. Onodera for the pGCDNsam-IRES-EGFP retroviral vector; R. Ono and T. Nosaka for the MLL-ENL cDNA; I. Kitabayashi for the MOZ-TIF2 cDNA; W. Hahn for the pBabe-GFP and pBabe-GFP-IκB-SR; and H. Algül and R.M. Schmid for providing the *Rela*-floxed mice. This work was supported by a Grant-in-Aid for Scientific Research A (KAKENHI 12020240) from the Ministry of Education, Culture, Sports, Science and Technology of Japan.

Received for publication December 3, 2012, and accepted in revised form October 17, 2013.

Address correspondence to: Mineo Kurokawa, Department of Hematology and Oncology, Graduate School of Medicine, The University of Tokyo, 7-3-1 Hongo, Bunkyo-ku, Tokyo 113-8655, Japan. Phone: 81.3.5800.9092; Fax: 81.3.5840.8667; E-mail: kurokawa-tky@umin.ac.jp.

1. Bonnet D, Dick JE. Human acute myeloid leukemia is organized as a hierarchy that originates from a primitive hematopoietic cell. *Nat Med.* 1997; 3(7):730–737.
2. Lapidot T, et al. A cell initiating human acute myeloid leukaemia after transplantation into SCID mice. *Nature.* 1994;367(6464):645–648.
3. Ishikawa F, et al. Chemotherapy-resistant human AML stem cells home to and engraft within the bone-marrow endosteal region. *Nat Biotechnol.* 2007; 25(11):1315–1321.
4. Marcucci G, Haferlach T, Döhner H. Molecular genetics of adult acute myeloid leukemia: prognostic and therapeutic implications. *J Clin Oncol.* 2011; 29(5):475–486.
5. Mardis ER, et al. Recurring mutations found by sequencing an acute myeloid leukemia genome. *N Engl J Med.* 2009;361(11):1058–1066.
6. Sen R, Baltimore D. Inducibility of kappa immunoglobulin enhancer-binding protein Nf-κB by a post-translational mechanism. *Cell.* 1986;47(6):921–928.
7. La Rosa FA, Pierce JW, Sonenshein GE. Differential regulation of the c-myc oncogene promoter by the NF-κB rel family of transcription factors. *Mol Cell Biol.* 1994;14(2):1039–1044.
8. Guttridge DC, Albanese C, Reuther JY, Pestell RG, Baldwin AS Jr. NF-κB controls cell growth and differentiation through transcriptional regulation of cyclin D1. *Mol Cell Biol.* 1999;19(8):5785–5799.
9. Duckett CS. Apoptosis and NF-κB: the FADD connection. *J Clin Invest.* 2002;109(5):579–580.
10. Karin M, Greten FR. NF-κB: linking inflammation and immunity to cancer development and progression. *Nat Rev Immunol.* 2005;5(10):749–759.
11. Karin M. Nuclear factor-κB in cancer development and progression. *Nature.* 2006;441(7092):431–436.
12. Pikarsky E, et al. NF-κB functions as a tumour promoter in inflammation-associated cancer. *Nature.* 2004;431(7007):461–466.
13. Guzman ML, et al. Nuclear factor-κB is constitutively activated in primitive human acute myelogenous leukemia cells. *Blood.* 2001;98(8):2301–2307.
14. Guzman ML, et al. Preferential induction of apoptosis for primary human leukemic stem cells. *Proc Natl Acad Sci U S A.* 2002;99(25):16220–16225.
15. Frelin C, et al. Targeting NF-κB activation via pharmacologic inhibition of IKK2-induced apoptosis of human acute myeloid leukemia cells. *Blood.* 2005;105(2):804–811.
16. Carvalho G, et al. Inhibition of NEMO, the regulatory subunit of the IKK complex, induces apoptosis in high-risk myelodysplastic syndrome and acute myeloid leukemia. *Oncogene.* 2007;26(16):2299–2307.
17. Guzman ML, et al. An orally bioavailable parthenolide analog selectively eradicates acute myelogenous leukemia stem and progenitor cells. *Blood.* 2007;110(13):4427–4435.
18. Jenkins C, et al. Nuclear factor-κB as a potential therapeutic target for the novel cytotoxic agent LC-1 in acute myeloid leukaemia. *Br J Haematol.* 2008;143(5):661–671.
19. Jin Y, et al. Antineoplastic mechanism of niclosamide in acute myelogenous leukemia stem cells: inactivation of the NF-κB pathway and generation of reactive oxygen species. *Cancer Res.* 2010;70(6):2516–2527.
20. Takahashi S, et al. Over-expression of Flt3 induces NF-κB pathway and increases the expression of IL-6. *Leuk Res.* 2005;29(8):893–899.
21. Liu S, et al. Sp1/NFκB/HDAC/miR-29b regulatory network in KIT-driven myeloid leukemia. *Cancer Cell.* 2010;17(4):333–347.
22. Nakagawa M, et al. AML1/RUNX1 functions as a cytoplasmic attenuator of NF-κB signaling in the repression of myeloid tumors. *Blood.* 2011; 118(25):6626–6637.
23. Eppert K, et al. Stem cell gene expression programs influence clinical outcome in human leukemia. *Nat Med.* 2011;17(9):1086–1093.
24. Sarry JE, et al. Human acute myelogenous leukemia stem cells are rare and heterogenous when assayed in NOD/SCID/IL2Rγc-deficient mice. *J Clin Invest.* 2011;121(1):384–395.
25. Liu T, et al. Functional characterization of meningioma 1 as collaborating oncogene in acute leukemia. *Leukemia.* 2010;24(3):601–612.
26. Kvinlaug BT, et al. Common and overlapping oncogenic pathways contribute to the evolution of acute myeloid leukemias. *Cancer Res.* 2011; 71(12):4117–4129.
27. Neering SJ, et al. Leukemia stem cells in a genetically defined murine model of blast-crisis CML. *Blood.* 2007;110(7):2578–2585.
28. Wang Y, et al. The Wnt/β-catenin pathway is required for the development ofleukemia stem cells in AML. *Science.* 2010;327(5973):1650–1653.
29. Hinz M, et al. Nuclear factor κB-dependent gene expression profiling of Hodgkin's disease tumor cells, pathogenetic significance, and link to constitutive signal transducer and activator of transcription 5a activity. *J Exp Med.* 2002;196(5):605–617.
30. Gentles AJ, Plevritis SK, Majeti R, Alizadeh AA. Association of a leukemic stem cell gene expression signature with clinical outcomes in acute myeloid leukemia. *JAMA.* 2010;304(24):2706–2715.
31. Kishore N, et al. A selective IKK-2 inhibitor blocks NF-κB-dependent gene expression in interleukin-1 β-stimulated synovial fibroblasts. *J Biol Chem.* 2003;278(35):32861–32871.
32. Algül H, et al. Pancreas-specific RelA/p65 truncation increases susceptibility of acini to inflammation-associated cell death following cerulein pancreatitis. *J Clin Invest.* 2007;117(6):1490–1501.
33. Beg AA, Finco TS, Nantermet PV, Baldwin AS Jr. Tumor necrosis factor and interleukin-1 lead to phosphorylation and loss of IκBα: a mechanism for NF-κB activation. *Mol Cell Biol.* 1993;13(6):3301–3310.
34. DeNardo DG, Coussens LM. Inflammation and breast cancer. Balancing immune response: crosstalk between adaptive and innate immune cells during breast cancer progression. *Breast Cancer Res.* 2007;9(4):212.
35. McLean MH, et al. The inflammatory microenvironment in colorectal neoplasia. *PLoS One.* 2011; 6(1):e15366.
36. Charles KA, et al. The tumor-promoting actions of TNF-α involve TNFR1 and IL-17 in ovarian cancer in mice and humans. *J Clin Invest.* 2009; 119(10):3011–3023.
37. Moore RJ, et al. Mice deficient in tumor necrosis factor-α are resistant to skin carcinogenesis. *Nat Med.* 1999;5(7):828–831.
38. Popivanova BK, et al. Blocking TNF-α in mice reduces colorectal carcinogenesis associated with chronic colitis. *J Clin Invest.* 2008;118(2):560–570.
39. Egberts JH, et al. Anti-tumor necrosis factor therapy inhibits pancreatic tumor growth and metastasis. *Cancer Res.* 2008;68(5):1443–1450.
40. Li J, et al. TNF-α induces leukemic clonal evolution ex vivo in Fanconi anemia group C murine stem cells. *J Clin Invest.* 2007;117(11):3283–3295.
41. Hoang T, Levy B, Ouetto N, Hainan A, Rodriguez-Cimadevilla JC. Tumor necrosis factor α stimulates the growth of the clonogenic cells of acute myeloblastic leukemia in synergy with granulocyte-macrophage colonystimulating factor. *J Exp Med.* 1989;170(1):15–26.
42. Khoury E, et al. Tumor necrosis factor alpha (TNF α) downregulates c-kit proto-oncogene product expression in normal and acute myeloid leukemia $CD34^+$ cells via p55 TNF alpha receptors. *Blood.* 1994;84(8):2506–2514.
43. Zhang B, et al. Altered microenvironmental regulation of leukemic and normal stem cells in chronic myelogenous leukemia. *Cancer Cell.* 2012; 21(4):577–592.
44. Kerbauy DM, Lesnikov V, Abbasi N, Seal S, Scott B, Deeg HJ. NF-κB and FLIP in arsenic trioxide (ATO)-induced apoptosis in myelodysplasticsyndromes (MDSs). *Blood.* 2005;106(12):3917–3925.
45. Adams J. The development of proteasome inhibitors as anticancer drugs. *Cancer Cell.* 2004;5(5):417–421.
46. Chen L, Madura K. Increased proteasome activity,

ubiquitin-conjugating enzymes, and eEF1A translation factor detected in breast cancer tissue. *Cancer Res.* 2005;65(13):5599–5606.
47. Stein SJ, Baldwin AS. Deletion of the NF-κB subunit p65/RelA in the hematopoietic compartment leads to defects in hematopoietic stem cell function. *Blood.* 2013;121(25):5015–5024.
48. Iversen PO, Wiig H. Tumor necrosis factor α and adiponectin in bone marrow interstitial fluid from patients with acute myeloidleukemia inhibit normal hematopoiesis. *Clin Cancer Res.* 2005; 11(19 pt 1):6793–6799.
49. Pronk CJ, Veiby OP, Bryder D, Jacobsen SE. Tumor necrosis factor restricts hematopoietic stem cell activity in mice: involvement of 2 distinct receptors. *J Exp Med.* 2011;208(8):1563–1570.
50. Taniguchi T, Takata M, Ikeda A, Momotani E, Sekikawa K. Failure of germinal center formation and impairment of response to endotoxin in tumor necrosis factor alpha-deficient mice. *Lab Invest.* 1997; 77(6):647–658.
51. Schmittgen TD, Livak KJ. Analyzing real-time PCR data by the Comparative C(T) method. *Nat Protoc.* 2008;3(6):1101–1108.
52. Jain AK, Bloom DA, Jaiswal AK. Nuclear import and export signals in control of Nrf2. *J Biol Chem.* 2005;280(32):29158–29168.

Cancer Research

NF-κB Activity Regulates Mesenchymal Stem Cell Accumulation at Tumor Sites

Ryosuke Uchibori[1], Tomonori Tsukahara[1], Hiroyuki Mizuguchi[4], Yasushi Saga[2], Masashi Urabe[1], Hiroaki Mizukami[1], Akihiro Kume[1], and Keiya Ozawa[1,3]

Abstract

Mesenchymal stem cells (MSC) accumulate at tumor sites when injected into tumor-bearing mice, perhaps offering cellular vectors for cancer-targeted gene therapy. However, the molecular mechanisms involved in MSC targeting the tumors are presently little understood. We focused on MSC–endothelial cell (EC) adhesion following TNF-α stimulation in an attempt to elucidate these mechanisms. Interestingly, stimulation of MSCs with TNF-α enhanced the adhesion of MSCs to endothelial cells *in vitro*. This adhesion was partially inhibited by blocking antibodies against vascular cell adhesion molecule-1 (VCAM-1) and very late antigen-4 (VLA-4). It is well known that TNF-α induces VCAM-1 expression via the NF-κB signaling pathway. Parthenolide has an anti-inflammatory activity and suppressed NF-κB activity by inhibition of IκBα phosphorylation after TNF-α stimulation and strongly inhibited TNF-α–induced VCAM-1 expression on MSCs. *In vivo* imaging using luciferase-expressing MSCs revealed that the bioluminescent signal gradually increased at tumor sites in mice injected with untreated MSCs. In contrast, we observed very weak signals at tumor sites in mice injected with parthenolide-treated MSCs. Our results suggest that NF-κB activity regulates MSC accumulation at tumors, by inducing VCAM-1 and thereby its interaction with tumor vessel endothelial cells. These findings have implications for the ongoing development of efficient MSC-based gene therapies for cancer treatment. *Cancer Res; 73(1); 364–72. ©2012 AACR.*

Introduction

Mesenchymal stem cells (MSC) are nonhematopoietic stem cells with high-proliferative potency and have the ability to differentiate into multiple lineages. They are detected in several adult and fetal tissues, including bone marrow, adipose tissue, and umbilical cord blood. MSCs have generated a great deal of interest in their potential use in regenerative medicine due to their ability to migrate to damaged tissues and to produce cytokines. Furthermore, MSCs can be easily genetically modified with viral vectors to be used as novel cellular vehicles in gene therapy protocols. MSCs are also used to treat severe acute GVHD, because they accumulate at inflammatory lesions and have immunomodulatory activity.

Interestingly, recent studies indicated that MSCs also have the ability to accumulate in tumors. Therefore, they can be used as cellular vehicles for cancer-targeted gene therapy. Intravenous injection of engineered MSCs expressing IFN-β was reported to inhibit the growth of melanoma pulmonary metastasis (1) and breast cancer (2) in mice and also prolonged the survival of mice with glioma xenografts (3). Furthermore, interleukin (IL)-12, which improves immune surveillance against cancer cells (4), and chemokine CX3CL1 (fractalkine), which is able to activate T cells and natural killer (NK) cells (5), were used as therapeutic molecules. We have also shown that retrovirus vector–producing MSCs also effectively inhibit tumor growth (6). In this context, treatment has been developed using retroviral vectors expressing the thymidine kinase of herpes simplex virus combined with the prodrug ganciclovir.

The ability of MSCs to specifically localize the multiple tumors, makes them extremely attractive for targeted cancer therapy. The most likely cause of preferential migration was considered to be the release of chemotactic gradients from tumor tissues. MSCs have a variety of chemokine and cytokine receptors and respond functionally to ligands *in vitro*. Tumors are known to produce a large amount of chemokines and cytokines, which could serve as ligands for the receptors on MSCs (7). Therefore, the mechanism of MSC accumulation at the site of tumors seems to be based on their migratory ability. Nevertheless, although various growth factors and chemokines, such as platelet-derived growth factor (PDGF), hepatocyte growth factor (HGF), and stromal cell–derived factor-1α (SDF-1α) may be involved, the detailed molecular mechanisms of MSC accumulation at tumors are poorly understood.

Authors' Affiliations: [1]Division of Genetic Therapeutics, Center for Molecular Medicine; [2]Department of Obstetrics and Gynecology; [3]Division of Hematology, Department of Medicine, Jichi Medical University, Tochigi; and [4]Department of Biochemistry and Molecular Biology, Osaka University, Osaka, Japan

Note: Supplementary data for this article are available at Cancer Research Online (http://cancerres.aacrjournals.org/).

Corresponding Author: Keiya Ozawa, Division of Genetic Therapeutics, Center for Molecular Medicine, Jichi Medical University, 3311-1 Yakushiji, Shimotsuke, Tochigi 329-0498, Japan. Phone: 81-285-58-7402; Fax: 81-285-44-8675; E-mail: kozawa@jichi.ac.jp

doi: 10.1158/0008-5472.CAN-12-0088

In the present study, we focused on MSC–endothelial cell (EC) adhesion following TNF-α stimulation in an attempt to elucidate the mechanism of MSC accumulation at tumors.

Materials and Methods

Cell culture

Bone marrow–derived human MSCs (Lonza Walkersville, Inc.) were cultured in mesenPRO RS medium (Invitrogen). HEK293-derived AD-293 cells (Stratagene), human embryonic fibroblasts WI-38 (RIKEN BRC), human colon adenocarcinoma cell lines SW480 (Cell Resource Center for Biomedical Research Institute of Development, Aging and Cancer, Tohoku University, Miyagi, Japan), and SW480/RFP that was generated by transduction of SW480 with red fluorescent protein-expressing retrovirus vectors (RV-RFP), were grown in Dulbecco's Modified Eagle's Medium (DMEM)/F-12 medium (Invitrogen) supplemented with 10% FBS, 100 U/mL penicillin, and 100 μg/mL streptomycin (P/S). Human endothelial progenitor cells (ApproCell Inc.) were cultured in endothelial progenitor cells grown medium (ApproCell Inc.). Human colon adenocarcinoma cell lines Colo205 (Cell Resource Center for Biomedical Research Institute of Development, Aging and Cancer Tohoku University) and Colo205/RFP that was generated by transduction with RV-RFP, were grown in RPMI medium (Invitrogen) supplemented with FBS and P/S. All cultures were kept in an incubator at 37°C and 5% CO_2.

Adenoviral vectors

Adenoviral vectors expressing a GFP were constructed by an improved *in vitro* ligation method (8, 9). The shuttle plasmid pHMCA5-GFP contains a CA promoter (a β-actin promoter/CMV enhancer with a β-actin intron), *GFP* gene, and a bovine growth hormone (BGH) polyadenylation signal, all of which are flanked by I-CeuI and PI-SceI restriction sites. I-CeuI/PI-SceI–digested pHMCA5-GFP was ligated with I-CeuI/PI-SceI–digested pAdHM4, resulting in pAdHM4-CAGFP. pAdHM41-K7-CAGFP was constructed by ligation of I-CeuI/PISceI–digested pHMCA5-GFP with I-CeuI/PI-SceI–digested pAdHM41-K7 (10). Viruses (Ad5-GFP and AdK7-GFP) were generated by transfection of PacI-digested pAdHM4-CAGFP and pAdHM41-K7-CAGFP, respectively, into AD-293 cells with SuperFect (Qiagen) according to the manufacturer's instructions. Each virus was purified by $CsCl_2$ step gradient ultracentrifugation followed by $CsCl_2$ linear gradient ultracentrifugation. Virus particles and biologic titers of each vector preparation were determined as described by Mittereder and colleagues (11). We also created Ad vectors expressing luciferase (Luc) using the shuttle plasmid pHMCA5-Luc, which contains the *Luc* gene derived from pELuc-test (Toyobo Co. Ltd.). MSCs and fibroblasts were seeded in culture plates or flasks at a density of 1×10^4 cells/cm^2, and the next day the cells were treated with each adenovirus vector for 1.5 hours. The medium containing the vectors was removed and replaced with fresh medium.

Animal models

All animal experiments were approved by the Jichi Medical University (Tochigi, Japan) ethics committee and carried out in accordance with the NIH Guide for the Care and Use of Laboratory Animals. To create tumor-bearing mice, SW480/RFP cells (3×10^6) were subcutaneously inoculated into 4- to 6-week-old male Balb/c nu/nu mice (Clea Japan Inc.). The mice were used for experiments 7 days after inoculation.

Immunohistochemistry

Cultured MSCs and fibroblasts were transduced with AdK7-GFP at a concentration of 3,000 virus particles per cell (vp/cell). Two days after transduction, cells were injected into the left ventricular cavities (1×10^6, day 0) of tumor-bearing mice. Mice were sacrificed on day 4, and 7-μm serial cryosections from frozen tissues were processed. Immunohistochemistry was conducted with fluorescein isothiocyanate (FITC)-conjugated anti-GFP antibody (ab6662; Abcam Inc.) on tumor cryosections to detect MSCs or fibroblasts. Nuclei were stained with 4′,6-diamidino-2-phenylindole (DAPI; Vector Laboratories, Inc.). Images were obtained with a fluorescence microscope (BZ-9000; Keyence). SW480/RFP cells (3×10^6) were subcutaneously inoculated into 4- to 6-week-old male Balb/c nu/nu mice. Mice were sacrificed on day 11, serial sections from tumor tissues were processed. Immunohistochemistry was conducted with anti-mouse CD34 monoclonal antibody (MEC14.7; GeneTex Inc.) on tumor section to detect tumor blood vessels. Histofine Simple Stain Mouse MAX PO (Nichirei Biosciences, Inc.) was used as a horseradish peroxidase–conjugated secondary antibody, and 3,3′-diaminobenzidine (DAB) solution was used for brown color development. Sections were then counterstained with Hematoxylin (Wako Pure Chemical Industries, Ltd.). Images were obtained with a fluorescence microscope (BZ-9000).

In vivo imaging of homing ability to tumors

Cultured MSCs and fibroblasts were transduced with AdK7-Luc at a concentration of 3,000 and 680 vp/cell, respectively. Two days after transduction, cells were injected into the left ventricular cavities (1×10^6, day 0) of tumor-bearing mice, and then optical bioluminescence imaging was conducted to periodically trace the cells using an *in vivo* imaging system (IVIS; Xenogen). To detect bioluminescence from MSCs or fibroblasts, the reporter substrate D-luciferin (Ieda Chemical Co., Ltd.) was injected into the mouse peritoneum (75 mg/kg body weight) for scanning. The luminescent intensity at tumor sites was analyzed using Living Image software (Xenogen).

In vitro migration assays

Cultured MSCs or fibroblasts were serum-starved for 12 hours. One hundred microliters of tumor conditioning medium (CM), or serum-free medium supplemented with PDGF-BB (10 ng/mL), HGF (30 ng/mL), fibroblast growth factor-β (FGF-β; 20 ng/mL), SDF-1α (150 ng/mL), VEGF-A (25 ng/mL), or monocyte chemoattractant protein-1 (MCP-1; 100 ng/mL) was added to the lower wells of migration chambers (8-μm pore size; Neuro Probe, Inc.); MSCs or fibroblasts (4×10^4) were added to the upper wells. All recombinant proteins were purchased from R&D systems Inc.. Medium alone (DMEM/F-12) was used as a negative control and treatment with 30% FBS was the positive control. After incubation for 24 hours at

37°C, cells were labeled with CyQUANT NF dye, and cells attached to the lower surface of the filters were detached with trypsin. Fluorescent intensity was measured using a fluoroscan, and the number of adherent cells was quantified using a standard curve constructed by a known number of cells.

Flow cytometric analysis of adhesion molecules

Cultured MSCs, fibroblasts or endothelial cells were stimulated with TNF-α and harvested by trypsinization. Cell aliquots were incubated with FITC-conjugated monoclonal antibodies (BD) against vascular cell adhesion molecule-1 (VCAM-1), CD49d, CD29 (Integrin-β1), and analyzed by flow cytometry (FACScan; BD Biosciences). For each analysis, an aliquot of cells was also stained with isotype control immunoglobulin G (IgG)–conjugated to FITC as a negative control.

Assay for TNF-α produced in tumor-bearing mice

SW480/RFP (3×10^6) cells were subcutaneously inoculated into nude mice. Seven days after inoculation, mice were anesthetized with an overdose of isoflurane inhalation. The blood was collected and allowed to coagulate overnight on ice. After centrifugation of the samples (2,000 × *g*, 30 minutes, 4°C), the serum was removed and stored at −70°C. Tumor, spleen, and liver tissues were homogenized in 1.5 mL of α-minimum essential medium using a tissue homogenizer. The homogenates were then centrifuged (2,000 × *g*, 30 minutes, 4°C), and the supernatant was removed and recentrifuged (14,000 × *g*, 30 minutes, 4°C). Serum and supernatants from tissue homogenates were kept at −70°C until use. TNF-α was assayed using a commercially available ELISA kit (mouse TNF-α Instant ELISA; Bender MedSystems) according to the manufacturer's protocols.

***In vitro* adhesion assays**

For adhesion assays, endothelial cells (at 4 passages) were cultured to confluence on fibronectin-coated 96-well plates (20 ng/mL; Sigma-Aldrich, Inc.) and treated with TNF-α (10 ng/mL) for 12 hours before assaying. MSCs and fibroblasts were treated with TNF-α (10 ng/mL) 12 hours before the adhesion assays and incubated with isotype control IgG or anti-VCAM-1 or very late antigen-4 (VLA-4; 10 μg/mL) monoclonal antibodies (mAb) for 1 hour. Cells were labeled with CyQUANT NF dye, and 1×10^4 cells were seeded onto endothelial cells. After 30 minutes of incubation at 37°C, wells were washed thoroughly 3 times with PBS to remove nonadherent cells. Fluorescent intensity was measured using a fluoroscan, and the number of adherent cells was quantified using a standard curve constructed by a known number of cells. In some experiments, MSCs and fibroblasts were pretreated for adhesion studies with one of the following substances: TNF-α (10 ng/mL), anti-VCAM-1 antibody (mouse monoclonal anti-rat, clone 5F10, 10 μg/mL, Eurogentec), or anti-VLA-4 antibody (mouse monoclonal anti-rat, clone 1A29, 10 μg/mL, Research Diagnostics).

Parthenolide treatment of MSCs

Parthenolide (Biomol) was reconstituted in dimethyl sulfoxide (DMSO; Sigma-Aldrich, Inc.) to a stock concentration of 0.4 mol/L and subsequently diluted in PBS. MSCs were treated with parthenolide (5 μmol/L) for 6 hours before experiments. To assess the effect of parthenolide treatment of transgene expression, cells were reseeded into 96-well plates, and luciferase assays were conducted using luciferase-expressing MSCs. Cell viability after parthenolide treatment was also examined with Cell Proliferation Kit II [2,3-bis[2-methoxy-4-nitro-S-sulfophenynl]H-tetrazolium-5 carboxanilide inner salt (XTT); Roche Diagnostics GmbH] according to the manufacturer's instructions.

Western blotting

Western blot analysis was conducted to measure the NF-κB pathways. Next, MSCs were pretreated with parthenolide or vehicle (DMSO) for 6 hours, and then cultured with TNF-α (10 ng/mL) for 3 minutes. Cells were lysed in radioimmunoprecipitation assay (RIPA) buffer containing protease inhibitor (Pierce Biotechnology). Protein extracts were electrophoresed on a 4% to 12% Bis–Tris gel (Invitrogen), and transferred to polyvinylidene difluoride (PVDF) membranes. Membranes were incubated in PVDF blocking reagent (TOYOBO), and then incubated with primary antibodies against the following proteins: IκBα, phospho-IκBα (Ser32), NF-κB p65, phospho-NF-κB p65 (Ser536), and α-tublin (Cell Signaling Technology), followed by incubation with horseradish peroxidase-conjugated goat anti-rabbit IgG or -mouse IgG1 secondary antibody, and detected using a Western blotting detection system (GE Healthcare).

Immunocytochemistry

To visualize p65 nuclear translocation, MSCs were pretreated with parthenolide or vehicle (DMSO) for 6 hours and then cultured with TNF-α (10 ng/mL) for 20 minutes. Cells were fixed with 4% fomaline and permiabilized with Triron-X 100. After washing with PBS, slides were incubated with rabbit anti-p65 antibody (Cell Signaling Technology), followed by incubation with Alexa Fluor 488–conjugated goat anti-rabbit IgG secondary antibody. The actin cytoskeleton was stained with Alexa Fluor 546–conjugated phalloidin (Invitrogen); nuclei were stained with 1,5-bis{[2-(di-methylamino) ethyl]amino}-4,8-dihydroxyanthracene-9,10-dione (DRAQ)-5 dye (Invitrogen). Cells were examined using Keyence BZ-9000.

Results

***In vivo* imaging of MSC accumulation in tumors**

We used bone marrow–derived human MSCs, which expressed characteristic phenotypic markers for MSCs and differentiated into adipocyte, osteocyte, and chondrocyte under specific culture conditions (Supplementary Fig. S1). Then, fiber-modified adenovirus vectors (AdK7) were used for efficient transduction of MSCs and fibroblasts in this study. When the cells were transduced with GFP-expressing AdK7 vectors at a density of 3,000 vp/cell, transduction efficiency was almost 100% (Supplementary Fig. S2A and S2B). The bioluminescent intensity of MSCs transduced with luciferase-expressing Ad vectors at 3,000 vp/cell was equal to that of fibroblasts transduced at 680 vp/cell (Supplementary Fig. S2C). Mice injected with GFP-expressing MSCs or fibroblasts were sacrificed 4 days after injection for immunohistochemical analysis.

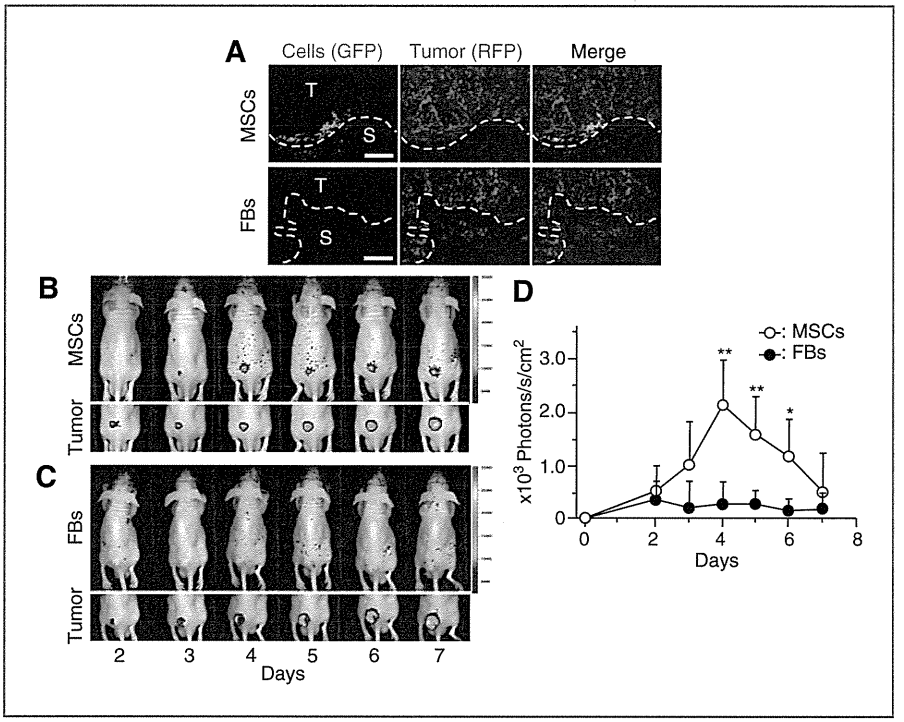

Figure 1. Tumor homing ability of MSCs *in vivo*. A, subcutaneous tumors were induced by injection of SW480/RFP cells (3×10^6) in nude mice (day 0). Cultured MSCs or fibroblasts were transduced with GFP-expressing adenovirus vectors 2 days before injection (day 5) and were injected into the left ventricular cavity (1×10^6, day 7). Mice were sacrificed on day 11, and immunohistochemistry was conducted with anti-GFP antibody on tumor cryosections to detect MSCs or fibroblasts. Top, fluorescent microscopy view of MSC detection; MSCs (left), RFP-labeled tumor cells (center), nucleic staining with DAPI and merge (right). Bottom, fluorescent microscopy view of fibroblast detection; fibroblasts (left), RFP-labeled tumor cells (center), nucleic staining with DAPI and merge (right). Data shown are from 1 representative experiment of 3 carried out. Scale bar, 100 μm. S, stroma; T, tumor. B, luciferase-expressing MSCs were injected into tumor-bearing mice via the left ventricular cavity (1×10^6, day 7). Optical bioluminescence imaging was conducted to periodically trace the cells using IVIS. Top, biodistribution of MSCs as detected by luminescence. Bottom, tumor site detected by red fluorescence. Data shown are from 1 representative experiment of 8 carried out. C, luciferase-expressing fibroblasts were injected into tumor-bearing mice and IVIS imaging was conducted as described earlier. Top, biodistribution of fibroblasts indicated by luminescence. Bottom, tumor site indicated by red fluorescence. Data shown are from 1 representative experiment of 7 carried out. D, bioluminescent intensity at tumor sites was quantified using analysis software. The data are expressed as mean ± SD ($n = 8$ for MSCs and $n = 7$ for fibroblasts). *, $P < 0.05$; **, $P < 0.01$ compared with fibroblasts at the same time.

MSCs identified with anti-GFP antibody were detected in the boundaries of tumors and tumor stroma. However, we found no GFP-positive fibroblasts in the tumor tissues (Fig. 1A). We also used bioluminescence imaging to quantitatively investigate the tumor tropism of MSCs. We injected luciferase-expressing MSCs or fibroblasts into mice through the left ventricular cavity, and then conducted optical bioluminescence imaging to periodically trace the cells using IVIS. In mice injected with luciferase-expressing MSCs, optical bioluminescence at tumor sites became pronounced over time (Fig. 1B), and signal intensity gradually increased (Fig. 1D). In contrast, we observed no signal at the tumor sites in mice injected with luciferase-expressing fibroblasts (Fig. 1C and D).

In vitro migration assays

We analyzed the effects of several growth factors (specifically PDGF-BB, HGF, and VEGF), chemokines (specifically MCP-1 and SDF-1α), and SW480 culture–conditioned medium on MSC and fibroblast migration. These factors are commonly expressed in tumor tissues, and are thought to be potential mediators of MSC tropism. We also used serum-free medium as a negative control and medium containing 30% FBS as a positive control. Migration was quantified by direct labeling and counting of cells by a fluorometer (Fluoroskan Ascent FL; Thermo Labsystems). Exposure to PDGF, HGF, or conditioned medium from SW480 cells stimulated significant MSC migration, whereas VEGF and SDF-1α had no significant effect as compared with serum-free medium (Fig. 2). We compared the migration capacity of MSCs and fibroblasts, the factors that attracted MSCs also induced migration of fibroblasts. Rather, it seems that fibroblasts were more strongly attracted to these factors than MSCs.

In vitro adhesion assays

The tumors generated in mice in this study strongly induced tumor stroma with defined blood vessels, and MSCs specifically accumulated in this stroma (Fig. 3A). Therefore, we propose a hypothesis as follows: factors, as indicated in Fig. 2, attract both MSCs and fibroblasts to the tumor microenvironment, but importantly, MSCs significantly adhere to endothelial cells as

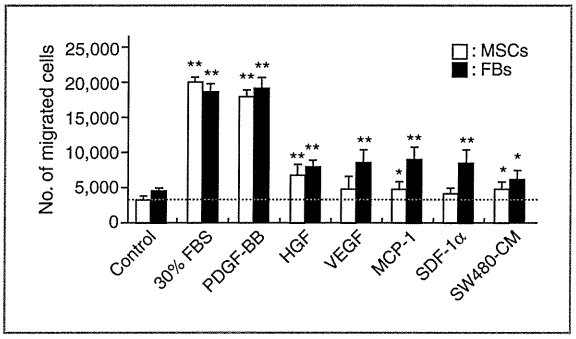

Figure 2. Migratory capacity of MSCs and fibroblasts (FB) in response to growth factors, chemokines, and conditioned medium from SW480 cells. MSCs or fibroblasts were serum-starved for 12 hours. Cells (4×10^4) were added to upper wells of migration chambers. Then, tumor conditioning medium, serum-free medium supplemented with PDGF-BB (10 ng/mL), HGF (30 ng/mL), SDF-1α (150 ng/mL), VEGF-A (25 ng/mL), or MCP-1 (100 ng/mL) were added to the lower wells. Treatment with medium alone (DMEM/F-12) was used as a negative control and treatment with 30% FBS was used as the positive control. The contents of the upper wells and lower wells were separated by polycarbonate filters (8 μm). The data are expressed as mean ± SD ($n = 8$ per cell type). Values are presented as mean ± SE. *, $P < 0.05$ and **, $P < 0.01$ compared with each control.

compared with fibroblasts. Therefore, only MSCs migrate and accumulate at tumor sites via blood vessels in tumor stroma. We speculated that inflammatory cytokines (specifically TNF-α) are required for induction of adhesion molecule expression. First, we measured TNF-α levels in tumor tissues by ELISA. The TNF-α level is significantly higher in tumor tissues as compared with liver and spleen (Fig. 3B). Similar results were also observed in another experiments using Colo205 tumor cells (Supplementary Fig. S3). Then, we assessed the expression of adhesion molecules on endothelial cells, MSCs, and fibroblasts by fluorescence-activated cell sorting analysis. After TNF-α stimulation, endothelial cells and MSCs significantly expressed adhesion molecules including VCAM-1 and VLA-4, compared with fibroblasts (Fig. 3C). We also examined the *in vitro* adhesion of MSCs to endothelial cells. MSCs effectively adhered to endothelial cells as compared with fibroblasts (Fig. 3D). Furthermore, this adhesion was partially inhibited by blocking antibodies against VCAM-1 and VLA-4.

Effects of parthenolide on MSC migration and adhesion

We propose a hypothesis that if TNF-α–induced VCAM-1 expression is inhibited, MSC accumulation at tumors is also attenuated. It is well known that TNF-α induces VCAM-1 expression through the NF-κB signaling pathway. We used parthenolide, a sesquiterpene lactone that occurs naturally in the Feverfew plant. Although parthenolide has several biologic activities, we focused on its suppressive effect on NF-κB activity. At first, there were no differences in migratory capacity toward growth factors or chemokines with or without parthenolide treatment (Fig. 4A). Next, we assessed the inhibitory effect of parthenolide on NF-κB activity: MSCs were pretreated for 6 hours, and then were stimulated with TNF-α for 3 minutes. Parthenolide suppressed p65 nuclear translocation through the inhibition of IκBα phosphorylation (Fig. 4B and C) and strongly inhibited the TNF-α–induced VCAM-1 expression on MSCs (Fig. 4D). Consequently, and MSC–EC adhesion was strongly inhibited by parthenolide treatment similarly to anti-VCAM-1 blocking antibody (Fig. 4E).

***In vivo* imaging of parthenolide-treated MSCs**

First, we examined the effect of parthenolide treatment on transgene expression and cell viability. There were no significant effects on transgene expression and cell viability after parthenolide treatment (Fig. 5A and B). Next, we conducted *in vivo* imaging using IVIS. We observed definite bioluminescence at tumor sites in the mice injected with untreated MSCs (Fig. 5C), and bioluminescent intensity was gradually increased (Fig. 5E), as indicated earlier (Fig. 1B). In contrast, we could not observe definite accumulation at the tumor sites in mice injected with parthenolide-treated MSCs (Fig. 5D and E). Similar results were also obtained by experiments using Colo205 tumor-bearing mice (Supplementary Fig. S4).

Discussion

In this study, we showed that MSC accumulation at tumor sites would be related not only to migratory capacity toward growth factors and chemokines, but also to MSC–EC adhesion following activation by TNF-α. We further showed that NF-κB activity regulates MSC accumulation at tumor sites through the induction of VCAM-1 expression and the resultant interaction with tumor blood vessel endothelial cells.

It is thought that MSCs are mobilized into action following tissue damage, such as injury or inflammation typically accompanied by the release of inflammatory cytokines from the damaged tissues, leading to the recruitment of MSCs to the target. Tumors have a microenvironment consisting of large numbers of inflammatory cells (12). This microenvironment promotes the recruitment of MSCs via various soluble factors secreted by the tumor and inflammatory cells, including EGF, VEGF-A, FGF, PDGF, SDF-1α, IL-8, IL-6, granulocyte colony-stimulating factor (G-CSF), granulocyte-macrophage colony-stimulating factor (GM-CSF), MCP-1, HGF, TGF-β1, and urokinase-type plasminogen activator (uPA; ref. 13). However, in our experimental settings, although systemically injected MSCs accumulated at the tumors, subcutaneously injected MSCs did not (data not shown). We also compared the migration capacity of MSCs and fibroblasts toward growth factors and chemokines *in vitro*. Rather, it seems that fibroblasts were more strongly attracted to these factors than MSCs. Our results suggest that the mechanism of MSC accumulation cannot be explained solely by cytokine-mediated migration. Therefore, we need different viewpoints to clarify the mechanism.

The tumors generated in this study strongly induced tumor stroma with large numbers of blood vessels, and MSCs in particular accumulated in the boundaries between the tumors and tumor stroma. Furthermore, MSC accumulation at the site of the tumors was observed only when cells were injected via the left ventricular cavity. Therefore, we focused on MSC–EC adhesion to elucidate the mechanisms involved.

It has previously been reported that the interaction of MSCs with the vascular endothelium resembles leukocyte chemotaxis (14). To analyze these interactions, we referred to a model

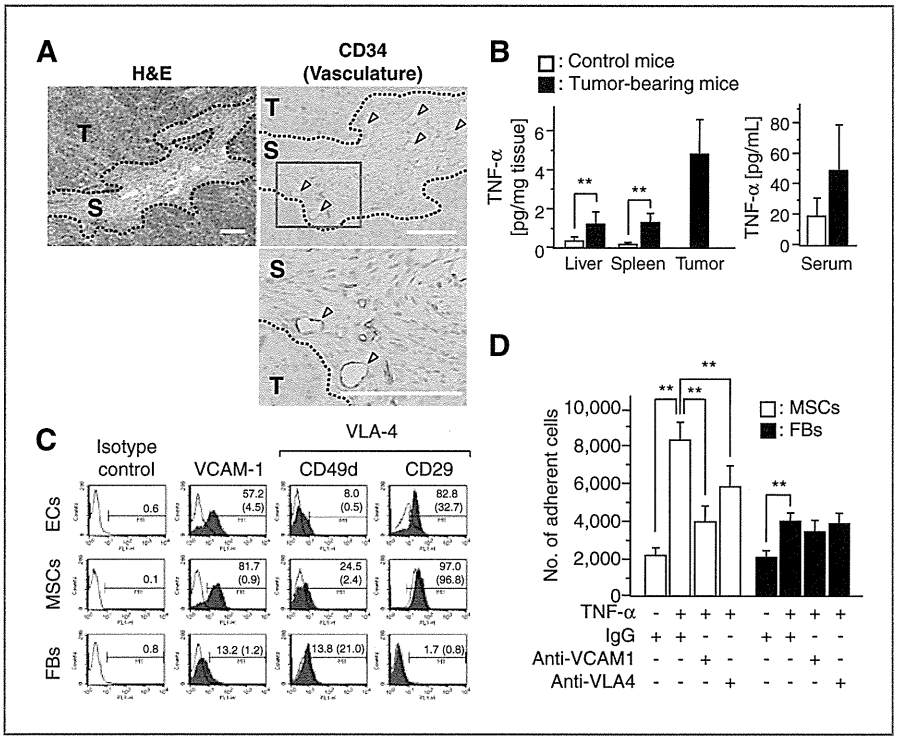

Figure 3. A, sections represent hematoxylin and eosin (H&E) staining (top left), the $CD34^+$ blood vessels/endothelial cells in tumor tissues (top right), the high-power field of view (bottom). Data shown are from 1 representative experiment of 3 carried out. Scale bar, 100 μm. S, stroma; T, tumor. B, specimens of tumor, liver, spleen, and blood were collected from control and tumor-bearing mice. TNF-α levels in tissue homogenates and serum were assayed by ELISA. *, $P < 0.05$; **, $P < 0.01$. C, MSCs, endothelial cells (EC), and fibroblasts were cultured with TNF-α (10 ng/mL) for 6 hours. Cells were labeled with FITC-conjugated antibodies and analyzed by flow cytometry (filled histogram). Rat isotype antibodies IgG1 and IgG2a served as respective controls (open histograms). Values represent the percentage of positive cells after TNF-α stimulation, and values in parentheses represent the percentage of positive cells without TNF-α stimulation. D, endothelial cells were cultured to confluence on fibronectin-coated 96-well plates. Then, MSCs or fibroblasts (1×10^4) were added to cultured endothelial cells. MSCs and endothelial cells were pretreated with the following substances: TNF-α (10 ng/mL), anti-VCAM-1, VLA-4 (10 μg/mL), or isotype control IgG. Values are mean ± SD. **, $P < 0.01$ ($n = 6$ per cell type).

that has been proposed for endothelial cell regulation of leukocyte infiltration in inflammatory tissues. Leukocyte-endothelial adhesion involves dynamic interactions between leukocytes and endothelial cells, and involves multiple steps. These steps must be precisely orchestrated to ensure a rapid response with minimal damage to healthy tissue (15). Interactions between leukocytes and the endothelium are mediated by several families of adhesion molecules, each of which participates in a different phase of the process. The surface expression and activation of these molecules during an inflammatory response is tightly controlled under normal conditions. Inflammatory cytokines including IL-1 and TNF-α involve induction of adhesion molecules. In our experimental settings, although other inflammatory cytokine levels including IL-1 and IL-6 were low (data not shown), significant production of TNF-α was observed. We do not clearly know the source of TNF-α in the tumor at this time, and that our *in vitro* data only suggest that the stroma is the primary source.

As we expected, TNF-α enabled MSCs to adhere to endothelial cells through induction of the expression of adhesion molecules, including VCAM-1 and VLA-4. It is generally considered that VCAM-1 on activated endothelium interacts with the VLA-4 on the leukocyte in the model of leukocyte–endothelial cell adhesion. At first, we speculated that VLA-4 on MSCs plays the same important role as leukocytes. Although both VCAM-1 and VLA-4 on endothelium were efficiently induced by TNF-α stimulation, TNF-α–induced expression of VCAM-1 on MSCs is much stronger than that of VLA-4. Furthermore, MSC–EC adhesion was more effectively inhibited by anti-VCAM-1 antibody as compared with the anti-VLA-4 antibody. On the basis of these results, although VLA-4 on MSC have also related to the MSC-EC adhesion, we thought that VCAM-1 on MSC has more important implications for this adhesion. Once MSCs circulate in the bloodstream, adhesion to endothelial cells is the first step in accumulation in tumors. TNF-α exerts its biologic functions through activating the NF-κB signaling pathway. NF-κB is a major cell survival signal that is antiapoptotic. MSC accumulation was significantly decreased through parthenolide inhibition of NF-κB activity. Although several studies have shown that mitogen-activated protein kinase (MAPK) phosphorylation by growth factors are involved in MSC migration (16, 17), parthenolide did not inhibit MAPK phosphorylation (data not shown). Therefore, at least parthenolide treatment did not affect in migration ability of

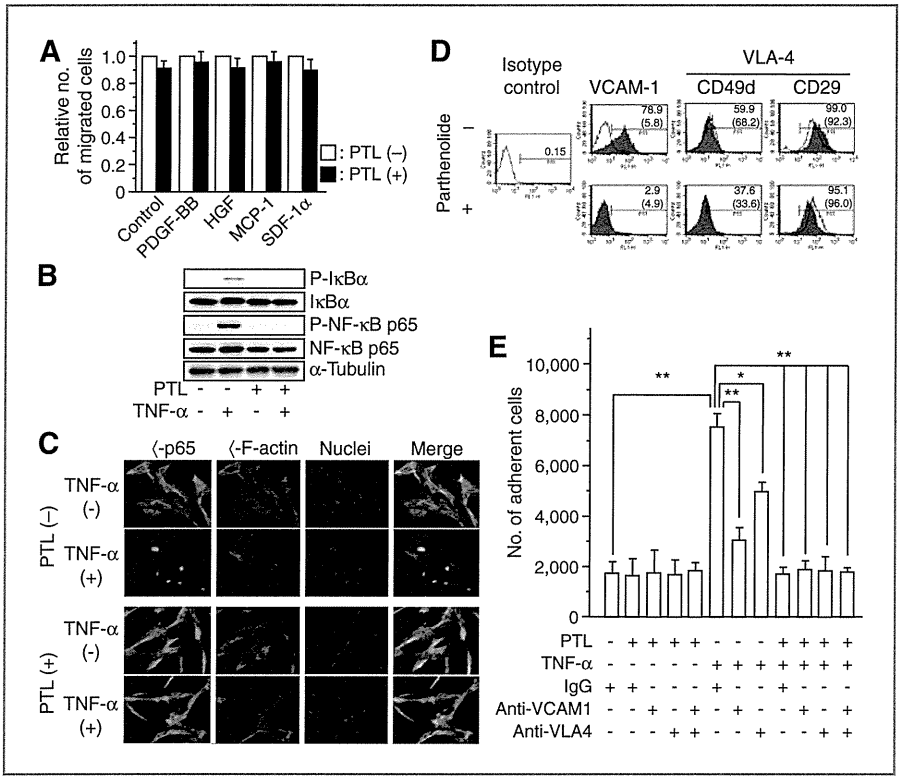

Figure 4. Effect of parthenolide (PTL) on MSC migration and adhesion. A, serum-starved and parthenolide-treated MSCs were added to the upper wells and serum-free medium supplemented with PDGF-BB (10 ng/mL), HGF (30 ng/mL), MCP-1 (100 ng/mL), or SDF-1α (150 ng/mL) was added to the lower wells. Treatment with medium alone (DMEM/F-12) was a negative control and treatment with 30% FBS was the positive control. Values are expressed by relative number of cells compared with respective controls (without pretreatment with parthenolide). B, to assess the inhibitory effect of parthenolide on NF-κB phosphorylation, parthenolide-treated MSCs were stimulated with recombinat TNF-α for 3 minutes, and cellular extracts were prepared for Western blotting. C, to monitor the inhibitory effect of parthenolide on NF-κB activation, immunofluorescent analysis of NF-κB p65 nuclear translocation was conducted as described in Materials and Methods with an Alexa Fluor 488–conjugated specific antibody (green). Actin filaments were labeled with Alexa Fluor 546–conjugated phalloidin (red); nuclei were stained with DRAQ-5 dye (blue). Objective magnification, ×40. D, effect of parthenolide treatment on TNF-α–induced expression of adhesion molecules was analyzed by flow cytometry. Parthenolide-treated MSCs were cultured with TNF-α (10 ng/mL) for 6 hours. Cells were labeled with FITC-conjugated antibodies and analyzed by flow cytometry (filled histogram). Rat isotype antibodies IgG1 and IgG2a served as respective controls (open histograms). Values represent the percentage of positive cells after TNF-α stimulation, and values in parentheses represent the percentage of positive cells without TNF-α stimulation. E, MSCs (1×10^4) were added to endothelial cells that had been cultured to confluence on fibronectin-coated 96-well plates. MSCs and endothelial cells were pretreated with the following substances: parthenolide (5 μmol/L), TNF-α (10 ng/mL), anti-VCAM-1, VLA-4 (10 μg/mL), or isotype control IgG. Values are expressed as mean ± SD ($n = 6$). *, $P < 0.05$ and **, $P < 0.01$.

MSCs toward growth factors from tumors in this experimental settings. Nevertheless, MSC accumulation was significantly decreased through parthenolide inhibition of NF-κB activity. We did not show histologic evidence in the experiments using parthenolide. However, we show that parthenolide does not inhibit luciferase activity *in vitro* (and thus does not seem to be toxic), and that therefore the effect observed *in vivo* should be an effect on recruitment. Although we focused on the function of TNF-α in this study, other inflammatory cytokines including IL-1β and IFN-γ also have ability to induce VCAM-1 expression in target cells (18), and may be involved in MSC accumulation.

TNF-α is a major inflammatory cytokine that plays important roles in diverse cellular events, such as cell survival, proliferation, differentiation, and death. Numerous reports have shown that TNF-α levels in serum are increased in patients with cancer (19, 20), and TNF-α is also related closely to the tumor progression including metastasis. For example, TNF-α intensely induces IL-6 and MCP-1 from cancer-associated fibroblasts and normal fibroblastic cells and has indirect influences on generation of prometastatic microenvironment (21). Furthermore, TNF-α is also released in cardiac infarction, during acute coronary syndromes, and in chronic heart failure; MSCs also accumulate at the site of cardiac infarction (22, 23). These results indicated that proinflammatory cytokines promote homing of stem cells in the heart and that these cytokines have a positive effect on cardiac regeneration. Therefore, activation with TNF-α is one of the critically important steps for MSC accumulation. Moreover, MSC-based tissue-targeted strategies may be adapted for various inflammatory diseases.

In MSC-based cancer-targeted gene therapies, it is thought that therapeutic efficacy is directly linked with accumulation efficiency of MSCs at tumor sites. Our results suggested that combination use of NF-κB inhibitors, including bortezomib, or TNF-α blocking agents, such as infliximab, reduces the

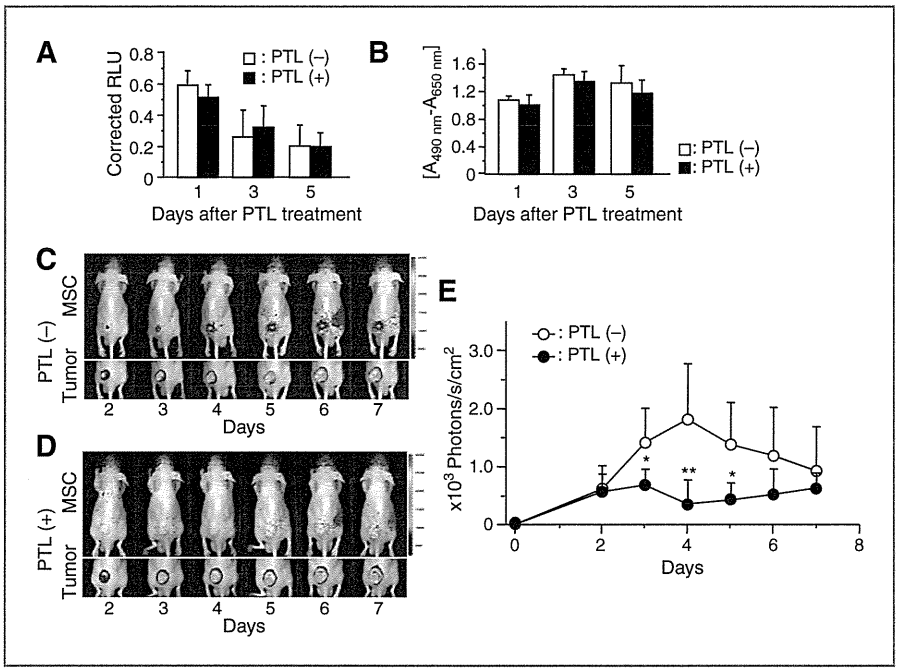

Figure 5. *In vivo* imaging of NF-κB–suppressed MSC accumulation at tumor sites. A, luciferase-expressing MSCs were cultured with parthenolide for 6 hours and luciferase assays were periodically conducted. Values are expressed as mean ± SD ($n = 4$ each). RLU, relative light unit. B, cell viability of parthenolide (PTL)-treated luciferase-expressing MSCs was also examined by XTT assays. Values are expressed as mean ± SD ($n = 4$ each). C, luciferase-expressing MSCs without parthenolide treatment were injected into tumor-bearing mice through the left ventricular cavity and IVIS imaging was periodically conducted. Each data shown are from 1 representative experiment of 8 carried out. D, luciferase-expressing MSCs with parthenolide treatment were injected into tumor-bearing mice and IVIS imaging was periodically conducted. Imaging was conducted as described earlier. Each data shown are from 1 representative experiment of 8 carried out. E, bioluminescent intensity at tumor sites was quantified using analysis software. The data are expressed as mean ± SD ($n = 8$ each). *, $P < 0.05$; **, $P < 0.01$ compared with a group of parthenolide (–) at the same time.

therapeutic efficacy of gene-modified MSCs due to inhibition of the accumulation steps. In contrast, tumor-specific TNF-α–inducing agents would be useful in enhancing therapeutic efficacy, thus further research is required in identifying such agents to more effective therapeutic strategies.

In conclusion, the present study shows that NF-κB activation through TNF-α stimulation and VCAM-1/VLA-4–mediated MSC-EC adhesion may be an important element in MSC accumulation. Although MSCs are useful as cellular vehicles for cancer-targeted gene therapy, past studies have shown that increased MSC accumulation is needed to enhance therapeutic efficacy. Thus, methodology for the enhancement of MSC accumulation should be developed and our findings suggest a solution.

Disclosure of Potential Conflicts of Interest

No potential conflicts of interest were disclosed.

Authors' Contributions

Conception and design: R. Uchibori, H. Mizukami, K. Ozawa
Development of methodology: M. Urabe
Acquisition of data (provided animals, acquired and managed patients, provided facilities, etc.): R. Uchibori
Analysis and interpretation of data (e.g., statistical analysis, biostatistics, computational analysis): R. Uchibori, H. Mizukami, A. Kume
Writing, review, and/or revision of the manuscript: R. Uchibori, M. Urabe, A. Kume
Administrative, technical, or material support (i.e., reporting or organizing data, constructing databases): T. Tsukahara, H. Mizuguchi, Y. Saga, K. Ozawa
Study supervision: M. Urabe, A. Kume, K. Ozawa

Acknowledgments

The authors thank Miyoko Mitsu for her encouragement and technical support.

Grant Support

This work was supported by Grant-in-Aid for Scientific Research (KAKENHI) from the Ministry of Education, Culture, Sports, Science and Technology (21390296 to K. Ozawa), and The Research Award to Jichi Medical School Graduate Student (to R. Uchibori).

The costs of publication of this article were defrayed in part by the payment of page charges. This article must therefore be hereby marked *advertisement* in accordance with 18 U.S.C. Section 1734 solely to indicate this fact.

Received January 13, 2012; revised August 30, 2012; accepted September 11, 2012; published OnlineFirst October 12, 2012.

References

1. Studeny M, Marini FC, Champlin RE, Zompetta C, Fidler IJ, Andreeff M. Bone marrow-derived mesenchymal stem cells as vehicles for interferon-beta delivery into tumors. Cancer Res 2002;62:3603–8.

2. Studeny M, Marini FC, Dembinski JL, Zompetta C, Cabreira-Hansen M, Bekele BN, et al. Mesenchymal stem cells: potential precursors for tumor stroma and targeted-delivery vehicles for anticancer agents. J Natl Cancer Inst 2004;96:1593–603.
3. Nakamizo A, Marini F, Amano T, Khan A, Studeny M, Gumin J, et al. Human bone marrow-derived mesenchymal stem cells in the treatment of gliomas. Cancer Res 2005;65:3307–18.
4. Chen X, Lin X, Zhao J, Shi W, Zhang H, Wang Y, et al. A tumor-selective biotherapy with prolonged impact on established metastases based on cytokine gene-engineered MSCs. Mol Ther 2008;16:749–56.
5. Xin H, Kanehira M, Mizuguchi H, Hayakawa T, Kikuchi T, Nukiwa T, et al. Targeted delivery of CX3CL1 to multiple lung tumors by mesenchymal stem cells. Stem Cells 2007;25:1618–26.
6. Uchibori R, Okada T, Ito T, Urabe M, Mizukami H, Kume A, et al. Retroviral vector-producing mesenchymal stem cells for targeted suicide cancer gene therapy. J Gene Med 2009;11:373–81.
7. Dwyer RM, Potter-Beirne SM, Harrington KA, Lowery AJ, Hennessy E, Murphy JM, et al. Monocyte chemotactic protein-1 secreted by primary breast tumors stimulates migration of mesenchymal stem cells. Clin Cancer Res 2007;13:5020–7.
8. Mizuguchi H, Kay MA. Efficient construction of a recombinant adenovirus vector by an improved *in vitro* ligation method. Hum Gene Ther 1998;9:2577–83.
9. Mizuguchi H, Kay MA. A simple method for constructing E1- and E1/E4-deleted recombinant adenoviral vectors. Hum Gene Ther 1999;10:2013–7.
10. Koizumi N, Mizuguchi H, Utoguchi N, Watanabe Y, Hayakawa T. Generation of fiber-modified adenovirus vectors containing heterologous peptides in both the HI loop and C terminus of the fiber knob. J Gene Med 2003;5:267–76.
11. Mittereder N, March KL, Trapnell BC. Evaluation of the concentration and bioactivity of adenovirus vectors for gene therapy. J Virol 1996;70:7498–509.
12. Coussens LM, Werb Z. Inflammation and cancer. Nature 2002;420:860–7.
13. Honczarenko M, Le Y, Swierkowski M, Ghiran I, Glodek AM, Silberstein LE. Human bone marrow stromal cells express a distinct set of biologically functional chemokine receptors. Stem Cells 2006;24:1030–41.
14. Rüster B, Göttig S, Ludwig RJ, Bistrian R, Müller S, Seifried E, et al. Mesenchymal stem cells display coordinated rolling and adhesion behavior on endothelial cells. Blood 2006;108:3938–44.
15. Butcher EC. Leukocyte-endothelial cell recognition: three (or more) steps to specificity and diversity. Cell 1991;67:1033–6.
16. Coffelt SB, Marini FC, Watson K, Zwezdaryk KJ, Dembinski JL, LaMarcad HL, et al. The pro-inflammatory peptide LL-37 promotes ovarian tumor progression through recruitment of multipotent mesenchymal stromal cells. Proc Natl Acad Sci U S A 2009;106:3806–11.
17. Zhang A, Wang Y, Ye Z, Xie H, Zhou L, Zheng S. Mechanism of TNF-α-induced migration and hepatocyte growth factor production in human mesenchymal stem cells. J Cell Biochem 2010;111:469–75.
18. Hosokawa Y, Hosokawa I, Ozaki K, Nakae H, Matsuo T. Cytokines differentially regulate ICAM-1 and VCAM-1 expression on human gingival fibroblasts. Clin Exp Immunol 2006;144:494–502.
19. Ferrajoli A, Keating MJ, Manshouri T, Giles FJ, Dey A, Estrov Z, et al. The clinical significance of tumor necrosis factor-alpha plasma level in patients having chronic lymphocytic leukemia. Blood 2002;100:1215–9.
20. Ahmed MI, Salahy EE, Fayed ST, El-Hefnawy NG, Khalifa A. Human papillomavirus infection among Egyptian females with cervical carcinoma: relationship to spontaneous apoptosis and TNF-alpha. Clin Biochem 2001;34:491–8.
21. Mueller L, von Seggern L, Schumacher J, Goumas F, Wilms C, Braun F, et al. TNF-alpha similarly induces IL-6 and MCP-1 in fibroblasts from colorectal liver metastases and normal liver fibroblasts. Biochem Biophys Res Commun 2010;397:586–91.
22. Shake JG, Gruber PJ, Baumgartner WA, Senechal G, Meyers J, Redmond JM, et al. Mesenchymal stem cell implantation in a swine myocardial infarct model: engraftment and functional effects. Ann Thorac Surg 2002;73:1919–25.
23. Pittenger MF, Martin BJ. Mesenchymal stem cells and their potential as cardiac therapeutics. Circ Res 2004;95:9–20.

Immunity
Article

The Satb1 Protein Directs Hematopoietic Stem Cell Differentiation toward Lymphoid Lineages

Yusuke Satoh,[1,7,8] Takafumi Yokota,[1,7,*] Takao Sudo,[1] Motonari Kondo,[2,9] Anne Lai,[2] Paul W. Kincade,[3] Taku Kouro,[4] Ryuji Iida,[3,4] Koichi Kokame,[5] Toshiyuki Miyata,[5] Yoko Habuchi,[1] Keiko Matsui,[1] Hirokazu Tanaka,[1,10] Itaru Matsumura,[1,10] Kenji Oritani,[1] Terumi Kohwi-Shigematsu,[6] and Yuzuru Kanakura[1]

[1]Department of Hematology and Oncology, Osaka University Graduate School of Medicine, Suita, Osaka 565-0871, Japan
[2]Department of Immunology, Duke University Medical Center, Durham, NC 27710, USA
[3]Immunobiology and Cancer Program, Oklahoma Medical Research Foundation, Oklahoma City, OK 73104, USA
[4]Laboratory of Immune Modulation, National Institute of Biomedical Innovation, Ibaraki, Osaka 567-0085, Japan
[5]Department of Molecular Pathogenesis, National Cerebral and Cardiovascular Center, Suita, Osaka 565-8565, Japan
[6]Department of Cell and Molecular Biology, Lawrence Berkeley Laboratory, University of California, Berkeley, Berkeley, CA 94720, USA
[7]These authors contributed equally to this work
[8]Present address: Department of Lifestyle Studies, Kobe Shoin Women's University, Kobe 657-0015, Japan
[9]Present address: Department of Immunology, Toho University School of Medicine, Tokyo 143-8540, Japan
[10]Present address: Division of Hematology, Department of Internal Medicine, Kinki University School of Medicine, Osaka 589-8511, Japan
*Correspondence: yokotat@bldon.med.osaka-u.ac.jp
http://dx.doi.org/10.1016/j.immuni.2013.05.014

SUMMARY

How hematopoietic stem cells (HSCs) produce particular lineages is insufficiently understood. We searched for key factors that direct HSC to lymphopoiesis. Comparing gene expression profiles for HSCs and early lymphoid progenitors revealed that Satb1, a global chromatin regulator, was markedly induced with lymphoid lineage specification. HSCs from Satb1-deficient mice were defective in lymphopoietic activity in culture and failed to reconstitute T lymphopoiesis in wild-type recipients. Furthermore, Satb1 transduction of HSCs and embryonic stem cells robustly promoted their differentiation toward lymphocytes. Whereas genes that encode Ikaros, E2A, and Notch1 were unaffected, many genes involved in lineage decisions were regulated by Satb1. Satb1 expression was reduced in aged HSCs with compromised lymphopoietic potential, but forced Satb1 expression partly restored that potential. Thus, Satb1 governs the initiating process central to the replenishing of lymphoid lineages. Such activity in lymphoid cell generation may be of clinical importance and useful to overcome immunosenescence.

INTRODUCTION

To maintain the immune system, hematopoietic stem cells (HSCs) differentiate to lymphoid-primed multipotent progenitors (LMPPs) and then to lymphoid-specified progenitors in a process accompanied by the loss of erythroid-megakaryocyte and myeloid potential (Adolfsson et al., 2005; Lai and Kondo, 2008). Accumulating evidence has suggested that combinations of transcription factors coordinately and sequentially regulate lymphopoiesis. Five transcription factors, PU.1, Ikaros, E2A, EBF, and Pax5 are hierarchically involved in the early steps of B-lineage differentiation (Medina et al., 2004). Whereas EBF and Pax5 specifically act in B-lineage-determined progenitors, PU.1 and Ikaros are expressed in earlier hematopoietic progenitors and involved in multiple lineage decision processes (Scott et al., 1997; Yoshida et al., 2006). E2A, an indispensable factor for B lymphopoiesis, can also affect T lymphocyte formation by regulating Notch1 expression (Ikawa et al., 2006). Furthermore, recent reports have shown that E2A proteins are expressed in primitive hematopoietic progenitors and play a critical role in early lymphoid specification (Dias et al., 2008; Yang et al., 2008; Semerad et al., 2009). However, whether the initiation of lymphoid differentiation is regulated entirely by transcription factors in a hierarchical manner remains unclear.

The immune system changes qualitatively and quantitatively with ontogeny and age (Miller and Allman, 2005; Montecino-Rodriguez and Dorshkind, 2006). Indeed, lymphocyte progenitors expand substantially in the fetal liver (FL), but their production shifts to bone marrow (BM) and becomes stable after birth. With age, replenishment of the adaptive immune system declines (Rossi et al., 2005; Sudo et al., 2000). Qualitative changes in lymphopoietic activity of HSCs are reflected in in vitro cell-culture experiments. If key inducers in early lymphoid lineages can be identified, they will be useful for expanding lymphocytes in culture for clinical purposes. Additionally, manipulating the expression of relevant genes might boost the immune system of immunocompromised and elderly people.

We have developed a method to sort early lymphoid progenitors (ELPs) from Rag1-GFP reporter mice (Igarashi et al., 2002; Yokota et al., 2003a). ELPs expressing Rag1 are present in the $Sca1^{+}c\text{-}kit^{hi}$ HSC-enriched fraction; they displayed high B and T lymphopoietic potential, but limited myeloerythroid potential and self-renewal ability. In contrast, $Rag1^{-}Sca1^{+}c\text{-}kit^{hi}$ HSCs effectively reconstitute and sustain the lymphohematopoietic system for long periods in lethally irradiated recipients. We conducted gene array comparisons between those two fractions

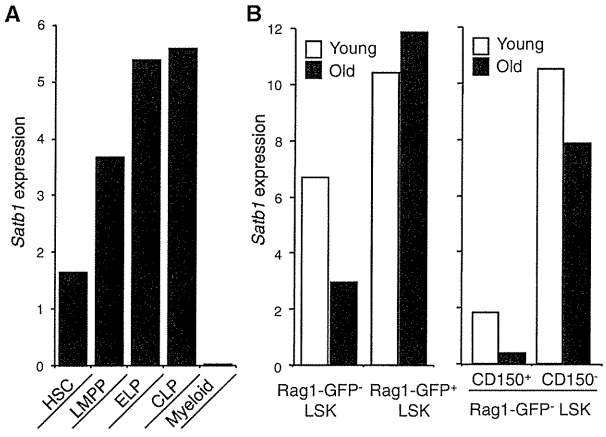

Figure 1. *Satb1* Expression Levels Change with Differentiation and Aging of HSCs

HSCs, LMPP, ELP, CLP, and the myeloid progenitor-enriched fractions were sorted from BM of 8- to 10-week-old Rag1-GFP knockin or WT mice according to cell surface markers and GFP expression (see Experimental Procedures), and transcripts for *Satb1* were quantitatively evaluated with real-time RT-PCR. (B) The LSK Rag1-GFP$^-$ and LSK Rag1-GFP$^+$ fractions (left panel) or the CD150$^+$ LSK Rag1-GFP$^-$ and CD150$^-$ LSK Rag1-GFP$^-$ fractions (right panel) were sorted from 6-week-old or 2-year-old Rag1-GFP knockin mice, respectively. Then *Satb1* expression was evaluated with real-time RT-PCR. The *Satb1* expression values were normalized by *Gapdh* expression and shown in each panel. Each data represents two independent examinations that showed essentially the same results (Figure 1; see also Figure S1 and Table S1).

with the goal of discovering molecules involved in the transition of HSCs to lymphoid lineages.

Herein, we showed that special AT-rich sequence binding 1 (Satb1), a nuclear architectural protein that organizes chromatin structure, plays an important role in lymphoid lineage specification. In parallel with or ahead of key transcription factors, the expression of Satb1 increased with early lymphoid differentiation. In functional assays, lymphopoietic activity was compromised in Satb1-deficient hematopoietic cells, but the induced expression of Satb1 strongly enhanced lymphocyte production from HSCs. Furthermore, exogenous Satb1 expression primed lymphoid potential even in embryonic stem cell (ESC)-derived mesoderm cells and aged BM-derived HSCs. Global analysis of potential Satb1 target genes identified a number that may have critical roles in early lymphopoiesis. The findings demonstrate that the earliest steps in lymphopoiesis are regulated by an epigenetic modifier and indicate how modulation of the process might be used to induce or rejuvenate the immune system.

RESULTS

Profiling Gene Expression of Rag1$^+$ ELP in Fetal Liver

We sorted the Rag1^{lo} c-kit^{hi} Sca1$^+$ ELP fraction and the Rag1$^-$ c-kit^{hi} Sca1$^+$ HSC-enriched fraction with high purity from E14.5 FL of Rag1-GFP knockin heterozygous embryos and performed gene arrays. We found that transcripts of *Trbv14* and *Ighm* genes were upregulated even in very early lymphoid progenitors (see Table S1 available online). Furthermore, we detected increased expression of *Il7r*, *Notch1*, and *Flt3* genes encoding cell surface receptors important for B or T lymphocyte differentiation in the ELP fraction. In addition to discovering many signal transduction kinases with unknown functions in lymphopoiesis, our search identified *Lck* and *Xlr4b* genes as being involved in lymphoid differentiation signals. Transcripts for some of these lymphoid-related genes had already been detected in the Rag1$^-$ HSC-enriched fraction (see the microarray data; accession number CBX73). These results suggest that lymphoid-lineage specification begins even before the emergence of Rag1^{lo} ELP. Additionally, the microarray data identified new candidate genes that might be important for early lymphoid development.

Expression of *Satb1* Increases with Early Lymphoid Specification and Declines with Age

Our major goal was to find key genes involved in the specification of lymphoid fates. Because the microarray data showed that expression of various lymphoid-related genes was activated before the ELP stage, we hypothesized the existence of a modulator that synchronously regulates multiple genes. Among the list in Table S1, *Satb1* attracted attention because it was originally identified as a protein binding to the enhancer region of the *Igh* gene and later shown to play a critical role in T cell development (Alvarez et al., 2000; Dickinson et al., 1992). Additionally, recent studies had demonstrated that it serves as a master regulator for many genes, including cytokines, cytokine receptors, and transcription factors (Cai et al., 2006; Han et al., 2008; Notani et al., 2010; Yasui et al., 2002).

To explore possible relationships between Satb1 and early lymphopoiesis, we examined its expression in primitive hematopoietic progenitors. The HSC-enriched Rag1-GFP$^-$ Flt3$^-$ lineage marker-negative (Lin$^-$) Sca1$^+$ c-kit^{hi} (LSK) fraction, the LMPP-enriched fraction, the ELP-enriched fraction, the common lymphoid progenitor (CLP)-enriched fraction, and the myeloid progenitor-enriched Lin$^-$ c-kit^{hi} Sca1$^-$ fraction were sorted from BM of 8- to 10-week-old mice. Transcripts for *Satb1* were then quantitatively evaluated with real-time RT-PCR. *Satb1* expression increased substantially when HSC differentiated into LMPP and ELP (Figure 1A). This trend matched that of other early lymphoid lineage-related genes including those that encode PU.1 (*Sfpi1*), Ikaros (*Ikzf1*), E2A (*Tcf3*), and Notch1 (Figure S1). Importantly, in contrast to its expression in the lymphoid lineage, *Satb1* expression was shut off when HSC differentiated to committed myeloid progenitors. These results suggest that *Satb1* is potentially involved in early lymphoid differentiation.

Lymphopoietic activity becomes compromised during aging. Accumulating evidence suggests that the earliest lymphoid progenitor pools proximal to HSC are deficient in aged BM (reviewed by Miller and Allman, 2005). Indeed, the Rag1$^+$ ELP population markedly decreases with age (data not shown). The downregulation of genes mediating lymphoid specification and function is likely a major cause (Rossi et al., 2005). Because *Satb1* has been listed in microarray panels as a downregulated gene in aged HSC (Chambers et al., 2007; Rossi et al., 2005), we sorted Rag1-GFP$^-$ LSK and ELP-enriched Rag1-GFP$^+$ LSK from BM of 6-week-old or 2-year-old Rag1-GFP heterozygous mice and examined their expression. In agreement with previous studies, our real-time RT-PCR identified an approximate 50% reduction of *Satb1* transcripts in aged Rag1-GFP$^-$ LSK cells (Figure 1B, left panel). The few ELP recovered from aged mice

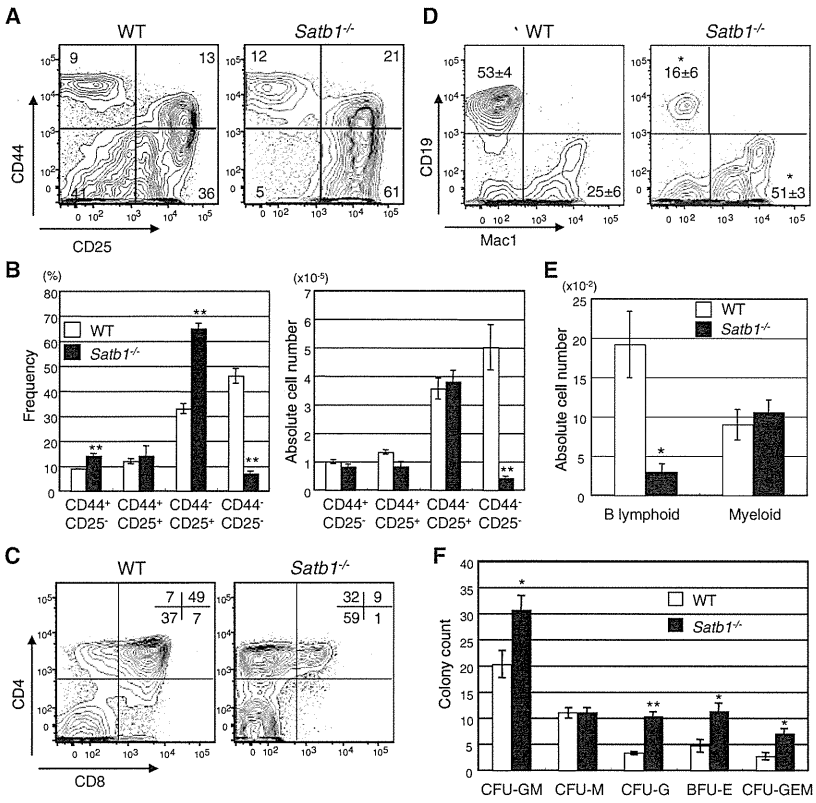

Figure 2. Satb1 Deficiency Alters Lymphoid and Myeloid Activities of Hematopoietic Stem/Progenitor Cells in Culture

Lin$^-$ cells were isolated from FL of E14.5 *Satb1*$^{-/-}$ embryos or their WT littermates.

(A–C) Cells were cocultured with OP9-DL1 stromal cells for evaluation of T-lineage differentiation. (A) Flow cytometry results are shown for cells recovered on day 14 and stained for CD44 and CD25/IL-2Rα. (B) Frequencies and absolute numbers of each phenotype were calculated. (C) A similar analysis was performed for CD4 and CD8α bearing cells recovered cells on day 18.

(D and E) The same cell suspensions were cocultured with MS5 stromal cells to assess B and myeloid lineage potentials and representative data are shown for day 7 of culture.

(F) In parallel, the Lin$^-$ cells were evaluated with methylcellulose colony assays. Each dish contained 1,000 sorted cells and colony counts were performed on day 10. The bars indicate numbers of CFU-GM, CFU-M, CFU-G, BFU-E, or CFU-GEM scored per dish. The results are shown as mean ± SE. Statistically significant differences between WT and *Satb1*$^{-/-}$ cells are marked with asterisks (*$p < 0.05$, **$p < 0.01$) (Figure 2; see also Figure S2).

expressed amounts of *Satb1* comparable to those in ELP from young mice. Recent purification methods for HSC with CD150, a SLAM family receptor that marks HSC even in aged BM (Yilmaz et al., 2006), identified an approximate 80% reduction in *Satb1* transcripts in aged HSC compared with ones from young mice (Figure 1B, right panel). These observations suggest that *Satb1* may be a key molecule related to immunosenescence.

Satb1 Deficiency Reduces the Lymphopoietic Activity of Hematopoietic Stem and Progenitor Cells

T cell development in the thymus is impaired in *Satb1*$^{-/-}$ mice (Alvarez et al., 2000). Although the profile of B220, immunoglobulin M (IgM), and IgD expression appears to be unaffected in the *Satb1*$^{-/-}$ spleen, the total number of B cells is reportedly reduced to approximately 25% of wild-type (WT) at 2 weeks of age (Alvarez et al., 2000). We have determined that the number and frequency of cells that can be recovered from lymphoid organs were reduced in E18.5–19.5 *Satb1*$^{-/-}$ fetuses. Body sizes of *Satb1*$^{-/-}$ fetuses were not different from WT and heterozygous littermates (Figures S2A and S2B).

We then sorted Lin$^-$ cells from FL of *Satb1*$^{-/-}$ mice or their WT littermates and cultured them with stromal cells that support lymphopoiesis. T cell differentiation can be recapitulated in vitro with hematopoietic cells cultured with OP9 expressing the Notch ligand Delta-like 1 (OP9-DL1). Under these coculture conditions, the differentiation patterns of WT and *Satb1*$^{-/-}$ Lin$^-$ cells differed significantly (Figures 2A and 2B). The majority of *Satb1*$^{-/-}$ cells were arrested in the CD44$^-$CD25$^+$ stage and did not differentiate into CD44$^-$CD25$^-$ cells. Reduction of IL-7 from culture media normally induces maturation of the CD4$^-$CD8$^-$ double-negative (DN) into CD4$^+$CD8$^+$ double-positive (DP) cells and subsequently into either the CD4$^+$ or the CD8$^+$ single-positive cells. However, more than half of the *Satb1*$^{-/-}$ cells were arrested in DN stages even after the IL-7 reduction, and their differentiation to the DP stage was aberrantly skewed toward CD4$^+$CD8$^-$ (Figure 2C).

Substantial differences were also observed in B-lineage cell production. In coculture with MS5, which supports B and myeloid lineages in the presence of SCF, Flt3-ligand, and IL-7, *Satb1*$^{-/-}$ progenitors exhibited significant reductions in B-lymphopoietic potential (Figures 2D and 2E). Coculture with OP9, which originated with M-CSF-deficient mice and supported the B lineage predominantly, also yielded reduced B/myeloid ratios with *Satb1*$^{-/-}$ progenitors (Figure S2C). Essentially the same results were obtained when cultures were initiated with LSK Flt3$^-$, more stringently purified HSC (Figure S2D, 2E). In addition, B cell lineage output was also reduced when *Satb1*$^{-/-}$ LMPP or CLP were cultured (Figure S2F). In contrast, the myeloid potential was retained in *Satb1*$^{-/-}$ progenitors (Figures 2D and 2E). Indeed, the Lin$^-$ fraction of E14.5 *Satb1*$^{-/-}$ FL contained more myeloid-erythroid progenitors than that of the WT control (Figure 2F).

In transplantation experiments, we observed that CD45.2$^+$ *Satb1*$^{-/-}$ HSC sorted from 2-week-old BM did not effectively reconstitute CD3$^+$ T-lineage cells in lethally irradiated CD45.1$^+$ WT recipients (Figure 3A). Peripheral blood CD3$^+$ T-lineage recoveries from *Satb1*$^{-/-}$ HSC were decreased approximately 90% compared with that from WT HSC (Figure 3B). Conversely, we observed varied amounts of reconstitution of the B lineage and no reduction in reconstitution of the myeloid lineage

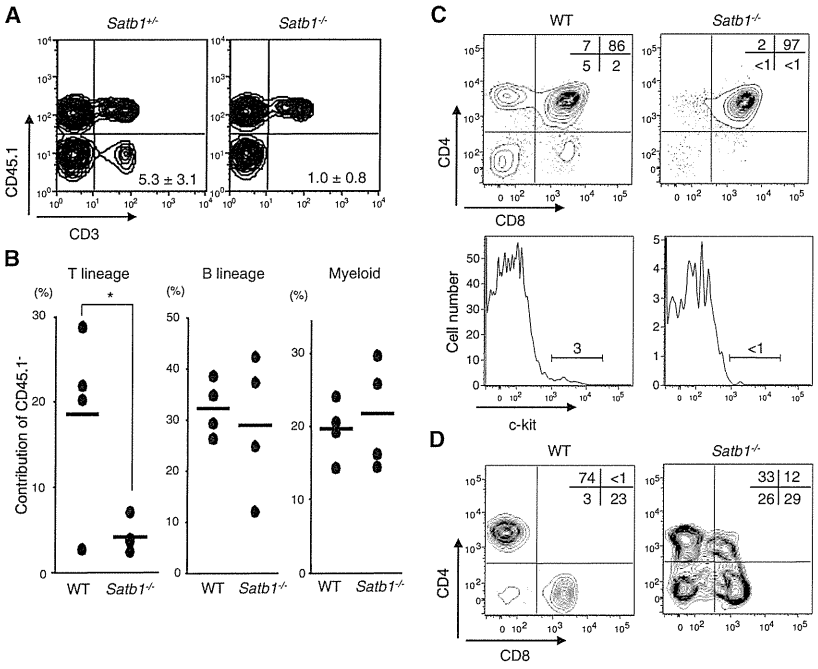

Figure 3. Defective T Lymphopoiesis from Transplanted *Satb1*$^{-/-}$ HSC

(A and B) One thousand stem-cell-enriched Flt3$^-$ LSK cells were sorted from BM of 2-week-old Satb1 deficient or littermate mice (CD45.2). They were then mixed with 4 × 10^5 adult BM cells obtained from WT (CD45.1) mice and were transplanted into lethally irradiated WT CD45.1 mice. At 8 weeks after transplantation, peripheral blood cells of the recipients were identified with anti-CD45.1 and anti-CD3. Numbers in each panel of (A) represent percentages of CD3$^+$ CD45.1$^-$ cells among the total leukocytes and are shown as averages with SD (n = 4 in each). Chimerisms of CD45.1$^-$ cells in the CD3$^+$ T-lineage, the CD45R/B220$^+$ B lineage, or the Gr1$^+$ myeloid lineage were determined. Statistical significance is *p < 0.05.

(C and D) One thousand Flt3$^-$ LSK cells sorted from E14.5 FL of Satb1 homodeficient or their WT littermates (CD45.2) were transplanted into lethally irradiated WT CD45.1 mice. At 8 weeks after transplantation, T-lineage reconstitution in the thymus and the spleen was analyzed. The CD4 and CD8 profiles of CD45.2$^+$ thymocytes (C, upper panels) and the c-kit expression of CD45.2$^+$ CD3$^-$ CD4$^-$ CD8$^-$ CD44$^+$ CD25$^-$ thymocytes (C; lower panels) are shown. (D) Representative CD4 and CD8 profiles are shown for CD45.2$^+$ CD3$^+$ cells in recipient spleens.

resulted from Satb1 ablation (Figure 3B). Compromised T cell lineage contributions of *Satb1*$^{-/-}$ HSC were also evident in the thymus and spleen (Figures 3C and 3D). Although T lymphopoiesis in the thymus was replaced by either WT or *Satb1*$^{-/-}$ donor cells when FL HSCs were transplanted, thymocytes were reduced in the *Satb1*$^{-/-}$ recipients and their differentiation was affected. Besides apparent stagnation at the DP stage and marked reduction of the DN population (Figure 3C, upper panels), c-kit^{hi} cells in the CD44$^+$CD25$^-$ DN1 stage were rare in *Satb1*$^{-/-}$ recipients (Figure 3C, lower panels). The reduced contribution of *Satb1*$^{-/-}$ cells was also evident in CD3$^+$ splenic T lymphocytes. Interestingly, T cells in the spleens of *Satb1*$^{-/-}$ recipients contained substantial percentages of DP and DN cells. Such T cell lineage cells are extremely rare in normal mouse spleens (Figure 3D).

Taken together, these results demonstrate that Satb1 is indispensable for normal T lymphopoiesis, but not for myelopoiesis. The factor may normally have a lesser role in B-lineage differentiation. Furthermore, our data indicate that abnormalities of lymphoid development observed in *Satb1*$^{-/-}$ mice are intrinsic to *Satb1*$^{-/-}$ hematopoietic cells.

Forced Expression of Satb1 in HSC Induces Lymphopoiesis

Next we conducted overexpression experiments to define the role of Satb1 in lineage-fate decisions of HSCs. LSK Flt3$^-$ cells were sorted from BM of adult WT mice and then retrovirally transduced with either a fluorescence-alone expressing control or a native Satb1 construct combined with a GFP-expressing vector. Successfully transduced cells were sorted according to GFP expression. Real-time RT-PCR and immunoblots revealed that Satb1-transduced cells expressed more than 10-fold *Satb1* transcripts and Satb1 proteins compared to control cells (Figure S3A).

The sorted cells were cultured with stromal cells that supported lymphopoieisis. Results from these experiments complemented the observations with *Satb1*$^{-/-}$ cells. Satb1 transduction enhanced T cell lineage growth in OP9-DL1 cocultures (Figures 4A and 4B). By day 10 of the culture, cells had been increased more than 5-fold by Satb1-transduction, and a majority of the recovered cells had progressed to the DN2 and DN3 stages. Differentiation to the DP stage was also advanced by the Satb1-transduction (Figure 4A). The kinetics of cell differentiation and expansion in the B cell lineage showed more changes. Whereas both control and Satb1-transduced cells produced substantial numbers of B-lineage cells, the latter produced B220$^+$CD19$^+$ cells more quickly and efficiently (Figure S3B). Specifically, the Satb1 transduction resulted in approximately 50- to 300-fold and 5-fold greater recovery of B220$^+$CD19$^+$ cells on day 10 in the MS5 and OP9 cocultures, respectively (Figures 4C and 4D). Notably, Satb1 transduction negatively influenced the output of myeloid cells, particularly Mac1^{lo}Gr1$^+$ granulocytes (Figure S3C). In addition, CFU-GM formation of HSC was decreased by Satb1 transduction (Figure S3D).

In stromal-free cultures containing SCF, Flt3-ligand, and IL-7, Satb1 expression strongly induced CD19$^+$ cell production from the LSK fraction (Figure S3E). When calculated on a per-cell basis, one LSK cell with Satb1 overexpression produced approximately 450 CD19$^+$ cells, whereas only 50 cells with this B-lineage marker were produced from control progenitors. As for other hematopoietic lineages, DX5$^+$CD3e$^-$ NK cells emerged when IL-15 was added to the stromal cell-free cultures. Coexpression of NK1.1 and/or CD94 confirmed the NK-lineage, and